Medium-Voltage Solid-State Transformer Design for Large-Scale H_2 Electrolyzers

Li, Z.; Mirzadarani, R.; Niasar, M. Ghaffarian; Itraj, M.; van Lieshout, L.; Bauer, P.; Qin, Z.

DOI
10.1109/OJPEL.2024.3414151

Publication date
2024

Document Version
Final published version

Published in
IEEE Open Journal of Power Electronics

Citation (APA)
Li, Z., Mirzadarani, R., Niasar, M. G., Itraj, M., van Lieshout, L., Bauer, P., & Qin, Z. (2024). Medium-Voltage Solid-State Transformer Design for Large-Scale H_2 Electrolyzers. *IEEE Open Journal of Power Electronics*, *5*, 936 - 955. https://doi.org/10.1109/OJPEL.2024.3414151

IEEE Open Journal of
Power Electronics

Received 13 March 2024; revised 26 April 2024 and 31 May 2024; accepted 10 June 2024. Date of publication 13 June 2024;
date of current version 26 June 2024. The review of this article was arranged by Associate Editor Zhixiang Zou.

Digital Object Identifier 10.1109/OJPEL.2024.3414151

Medium-Voltage Solid-State Transformer Design for Large-Scale H_2 Electrolyzers

Z. LI [1] (Student Member, IEEE), R. MIRZADARANI [1] (Student Member, IEEE), M. GHAFFARIAN NIASAR [1] (Member, IEEE), M. ITRAJ [2], L. VAN LIESHOUT [2], P. BAUER [1] (Senior Member, IEEE), AND Z. QIN [1] (Senior Member, IEEE)

[1] Department of Electrical Sustainable Energy, TU Delft, 2628 CD Delft, The Netherlands
[2] VONK, 8025 BS Zwolle, The Netherlands

CORRESPONDING AUTHOR: Z. QIN (e-mail: z.qin-2@tudelft.nl)

This work was supported the RVO MOOI (Missiegedreven Onderzoek Ontwikkeling en Innovation) under Grant Agreement MOOI 52103.

ABSTRACT In the production of green hydrogen, electrolyzers draw power from renewable energy sources. In this paper, the design of Solid State Transformer (SST) for large-scale H_2 electrolyzers is benchmarked. The three most promising topologies are chosen for design and comparison, including Modular Multi-level Converter (MMC) based SST, Modular Multi-level Resonant (MMR) based SST, and Input-Series-Output-Parallel (ISOP) based SST. The distance between converter towers for insulation and maintenance, the insulation system of the transformer, and the cooling system are designed with practical considerations in order to have an accurate estimation of the volume and weight of the SST. Losses in the switches are calculated based on equations, and losses in passive components are calculated based on FEM simulation. The operating frequency for each topology is optimized to minimize loss, weight, and volume. The best of each topology is then compared with each other to identify the most suitable one for large-scale H_2 electrolyzers.

INDEX TERMS Hydrogen electrolyzer, input-series-output-parallel (ISOP), modular multi-level converter (MMC), solid-state transformer.

I. INTRODUCTION

Green hydrogen is globally recognized as a pivotal solution, if not the sole one, for advancing renewable installations and circumventing grid congestion [1], [2]. For Green hydrogen, electrolyzers draw power from renewable sources. Green hydrogen can be further utilized in diverse applications, including the petroleum industry, transportation, and power generation via fuel cells or internal combustion engines. Moreover, hydrogen is seen as an eco-friendly energy storage solution due to its minimal environmental impact. Excess renewable energy can be efficiently converted and stored as hydrogen for later usage.

Typically, electrolyzers operate at tens of megawatts per unit, yet their input voltage is merely a few hundred volts DC. A transformer is essential to step down the voltage from a medium voltage bus, followed by the application of a rectifier to convert it to DC. The conventional solution often employs line frequency transformers plus diode rectifiers or thyristor rectifiers [3]. While these topologies have relatively low component costs, they tend to result in bulky overall systems. This is primarily attributed to the inclusion of line frequency transformers. In specific application scenarios where system size is of paramount importance, these conventional topologies are unacceptably large.

SST (Solid-State Transformer), on the other hand, is a promising solution to size and weight-restricted scenarios, e.g., tractions [4], nacelles of wind turbines [5], [6], future navy warships [7], underground distribution networks [8], etc. The concept of SST involves initially transforming line frequency power into medium- or high-frequency by using power converters. Subsequently, this allows for voltage conversion and galvanic isolation using a medium frequency transformer, which is notably more compact and lighter than conventional line frequency transformers. While this idea is not novel, it has recently gained increased interest and is emerging as a promising technology, particularly for

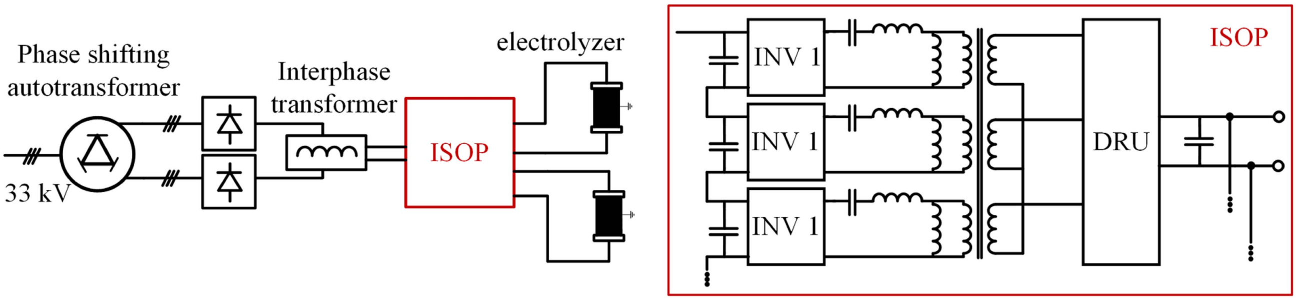

FIGURE 1. Cascaded structure SST for electrolyzer application. Instead of isolated transformer, autotransformer is used to generate the 30° phase shift angle for two DRUs, to save space and weight. The DC-DC cascaded structure uses three phase LLC modules with input series output parallel connection.

medium-voltage applications, because significant advancements in semiconductor power switch manufacturing have enhanced power density, switching frequencies, and energy efficiency.

Different topologies are feasible for SST, and one frequently mentioned topology in the literature is the cascaded structure [9], [10]. The primary advantage of a cascaded structure lies in its modularity, which renders it versatile for various application scenarios with diverse voltage and current requirements.

In applications involving large-scale electrolyzers, the power conversion process commonly involves converting medium voltage input to low voltage output. For such scenarios, as depicted in Fig. 1, adopting an ISOP (Input-Series Output-Parallel) configuration is deemed more advantageous. For power module selection, the Dual Active Bridge (DAB) converter and resonant converters are commonly employed. However, for unidirectional power flow applications in electrolyzers, the DAB's bidirectional capability is excessive, and its higher number of active switches leads to increased costs. Therefore, LLC resonant converters, being more cost-effective and efficient for such applications, are considered a better fit. Additionally, a twelve-pulse Diode Rectifier Unit (DRU) is employed for cost-effective medium voltage AC to DC conversion. A more detailed analysis and discussion will be provided in Section IV.

The primary limitation of the ISOP configuration lies in its requirement for numerous low-power transformers. These transformers must be isolated to withstand the entire high-level DC voltage, leading to significant increases in both volume and cost due to the extensive need for isolation and insulation in their design. On the contrary, another suitable topology, Modular Multi-level Converter (MMC) based SST [11], [12], [13], as shown in Fig. 2, tries to use central medium frequency transformers to solve the problems above for a more compact solution. A comparison between five different MMC-based SST topologies for AC-DC electrolyzer applications is conducted in [14]. DRU – three phase MMC-based SST is considered the best topology from the semiconductor rating and capacitor rating requirement point of view. Thus, this topology is analyzed in detail in Section II.

To reduce the switching losses of MMC-SST in medium and high-frequency applications, Modular Multi-level Resonant (MMR) converter is an effective solution [15], [16]. as shown in Fig. 2. The MMR resembles two-level resonant converters, e.g., LLC, where a string of modules replaces the single active switch in each bridge in the primary side. The overall structure is similar to MMC. However, additional resonant capacitors are inserted, and the modulation method is different.

Several studies have conducted comparative analysis on the topologies mentioned above [17], [18]. References [19], [20] theoretically analyze the high insulation requirement drawback of the cascaded structure. However, no detailed calculations are presented. An assessment of charging station converter structures is carried out in [21] by using MMC as an active front-end rectifier in three different topologies. However, the transformer size and insulation distance are not considered. References [22], [23] compared cascaded SST and MMC-SST, focusing only on the power converter parts analysis. Despite extensive studies in the field, there remains a noticeable lack of quantitative analysis comparing different SST topologies, especially regarding their insulation requirements.

The contributions of this paper are:

1) This paper conducts a comprehensive quantitative comparison of MMC-based, MMR-based, and ISOP SSTs for electrolyzer applications, evaluating them from the perspectives of efficiency, size, and weight. This comparison provides valuable insights into the optimal choice of SST topology based on specific application requirements.
2) Detailed calculations of the size and weight of converter towers and transformers are performed, incorporating practical considerations such as insulation distance requirements. This approach ensures a realistic assessment of the spatial and structural implications of each SST topology.
3) The analysis identifies the significant impact of chiller size and weight in the overall size and weight comparison, highlighting the importance of cooling systems in the efficiency and feasibility of converter and medium frequency transformer designs.

To begin with, Section II first introduces the components of the MMC-SST and the parameter design methods. Power converter and transformer loss, size, and weight estimations

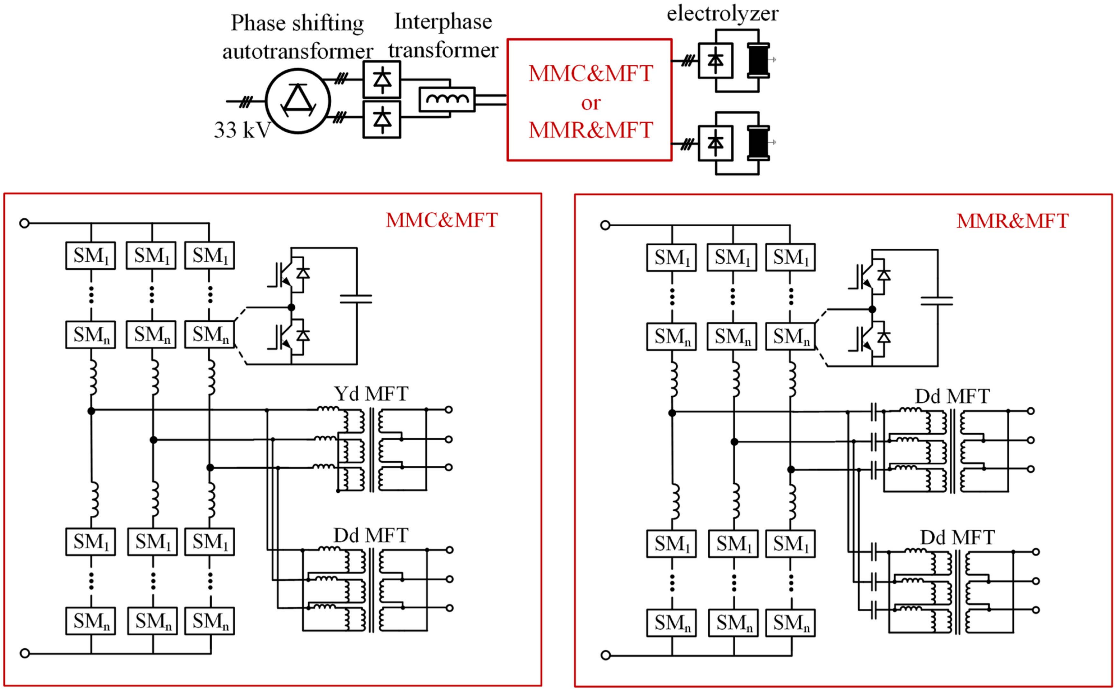

FIGURE 2. MMC-based and MMR-based SST configurations. Both systems utilize a DRU setup similar to the cascaded structure SST. The MMC-SST employs a Yd and Dd MFTs configuration, creating a twelve-pulse structure that reduces conduction losses in the MMC. The MMR working principle resembles the two level three phase LLC converter, utilizing two Dd MFTs. Due to the sinusoidal resonant currents of the MMR, which inherently have low THD, the necessity for a twelve-pulse configuration is eleminated.

are carried out consecutively. A comparison of the performance metrics at different frequencies is shown to decide the optimal operating frequency of the MMC-SST. Following a similar procedure, Sections III and IV indicate the MMR and ISOP SST loss, size, and weight estimations and these values at different frequencies, respectively. Additionally, Section V presents an analysis of the frequency sweep results and a comparison of the three topologies at their optimal operating frequencies. The paper concludes with Section VI.

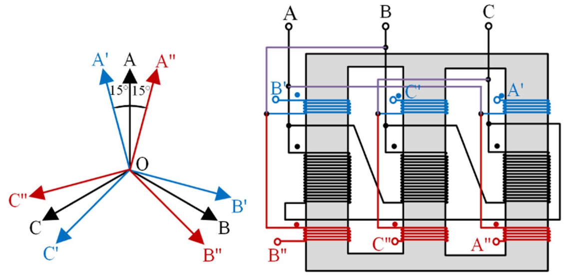

(a)

(b)

FIGURE 3. (a) Autotransformer vector graph. A′ and A″ represent the generated phase A voltages with a 30° phase shift. (b) Windings of an autotransformer on a three-limb core.

II. PERFORMANCE METRICS FOR MODULAR MULTI-LEVEL CONVERTER BASED SOLID-STATE TRANSFORMER

A. PARAMETER DESIGN OF THE COMPLETE SYSTEM

The complete system, which includes two electrolyzers, has a total power rating of 45.4 MW. For this application, the input current ripple to the electrolyzer must be confined to within 3%. Exceeding this threshold can reduce the lifespan of the electrolyzer and adversely affect the rate of hydrogen production. This requirement will be addressed in the subsequent design phase.

1) 12-PULSE RECTIFIER SYSTEM

To satisfy the IEC61000-3-6 current harmonics requirements of the 33 kV grid, a 12-pulse rectifier circuit should be used. To generate the $\pm 15^\circ$ voltage phase shift, usually a 3-winding isolated transformer is used. However, because of the isolation functionality and the fact that 50Hz is implemented as the operating frequency, this isolated transformer will be bulky and heavy. To fulfill the purpose of size and weight reduction of solid-state transformers, autotransformer can be used where there is no isolation between the windings. The vector diagram and the configuration are shown in Fig. 3(a) and (b).

Based on the autotransformer vector diagram, the voltage transfer ratio of the 12-pulse autotransformer can be derived as $1/\cos(15^\circ) = 1.0353$.

Following the autotransformer, two 6-pulse diode rectifiers are connected to the output of the autotransformer. The voltage transfer ratio of the 6-pulse diode rectifier from the input three phase AC line to line peak voltage to output DC voltage is $3/\pi$. Diodes selection method is as follows: first, the diode

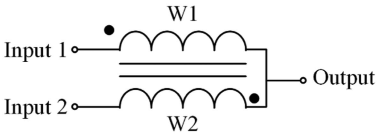

FIGURE 4. Interphase transformer diagram. W1 and W2 represents the two windings of the interphase transformer.

peak reverse voltage and average current are measured in the simulation, which are 48.3 kV and 300 A, respectively. Then, a voltage safety factor of 2.25 and a current safety factor of 2 are applied, according to [24]. If the Infineon D471N diode with a voltage rating of 9000 V and current rating of 600A is selected, then for each bridge $ceil\ (48.3\ kV \times 2.25/9\ kV) =$ 13 diodes should be series connected.

The interphase transformer facilitates the parallel connection of two diode bridges, each fed by voltage sources with a phase difference [25]. Specifically, two interphase transformers are needed in our applications: one for each voltage polarity. The configuration of an interphase transformer and its associated connections are depicted in Fig. 4.

As a result, the output DC voltage of the interphase transformer is $U_{dc} = 33 \times \sqrt{2} \times 3/\pi \times 1.0353 = 46.2\ kV$.

2) MMC SYSTEM

The MMC design follows the design guidelines in [26], [27]. MMC's initially selected fundamental frequency is 400Hz, but the design process could also be applied to other frequencies.

The maximum modulation index corresponding to the maximum operating point of the electrolyzer is set as 0.9 to leave a certain safety margin. The maximum arm current value according to simulation is 1050A. With a current safety factor of 2, the 3.3 kV 1.2 kA ABB 5SNA 1200E330100 IGBT with a peak collector current of 2400A is chosen, and the voltage rating is derated to 2 kV to have a safe margin for potential transient voltages. The number of submodules is calculated as 24. The submodule is half bridge submodule, since in this SST application, the MMC DC side short circuit fault is unlikely to happen compared with HVDC applications. The submodule capacitance is chosen as 1.45 mF to ensure that the submodule voltage variation is within the limit and the IGBT's power loss is minimal.

The arm inductance is calculated based on [27] as 0.9 mH. In this study, the losses attributed to arm inductance are neglected, as they contribute to only approximately 0.02% of the Modular Multi-level Converter's (MMC) rated power, according to [27].

Different modulation methods for MMC exist, including carrier-based PWM and Nearest Level Control (NLC) method. To reduce the unnecessary switching behavior and increase the efficiency, NLC plus advanced sorting algorithms have been applied to the MMC, i.e., the cell tolerance band (CTB) method [27]. Fig. 16(a) displays the submodule voltage waveforms, demonstrating the effectiveness of the CTB method. Additionally, Fig. 16(b) illustrates the MMC output currents with low harmonic content.

3) MEDIUM FREQUENCY TRANSFORMER

The medium-frequency transformer (MFT) is designed based on IEC 60076 [28]. The 12-pulse behavior seen by the MMC output is realized by phase shifting the transformer's primary windings. And there are two MFTs, one with Yd connection and another with Dd connection. According to the power limit per transformer in IEC 60076, and the demand of the two electrolyzers, the oil-immersed transformers with two active parts in one tank is chosen. Section II-D will elaborate on the transformer design.

4) MEDIUM FREQUENCY DRU RECTIFIER

Two 6-pulse medium frequency DRUs are connected to the output of the MFT. The measured peak reverse voltage is 800V, and the average current is 12kA. With the same 2.25 voltage safety factor and 2 current safety factors, the 5SDF28L4521 medium frequency diode with a voltage rating of 4500V and current rating of 2620A is chosen, and for each bridge, a total of 10 diodes should be parallel connected. To ensure the electrolyzer input current ripple remains within the required 3%, a 50 μH inductor has been integrated prior to the connection with the electrolyzer. The resulting input current waveform is depicted in Fig. 16(c), demonstrating compliance with the ripple specifications.

B. THERMAL MODELLING AND LOSS ESTIMATION OF POWER CONVERTERS

The loss estimations for power converters in MMC-SST include 50 Hz DRU losses, MMC losses, and medium frequency DRU losses. Thermal models are built in Simulink to calculate these losses.

For the 12-pulse DRU, only conduction losses need to be considered because of the main frequency operation, based on [24]. The equation to calculate the conduction losses is [24]:

$$P_{loss} = U_{T0} \times I_{FAV} + r_T \times I_{Frms}^2 \tag{1}$$

where I_{FAV} is the average current through the diode, and I_{Frms} *is* the root mean square value of the current. The threshold voltage U_{T0} and the slope resistance r_T are given in the datasheet. For the cooling design, one needs to make sure that the junction temperature of the devices should be within 125°C measured from thermal modelling, thus, the switches will not be damaged during operation. Due to the low losses in the DRU, forced air cooling is enough for the DRU, and the heatsink of ASENERGI O343 with a thermal resistance of 0.1 K/W is chosen.

For MMC losses calculation, the IGBT/diode thermal resistance, thermal capacitance, turn-on, turn-off, and on-state characteristics are imported from the switch datasheet. And the junction temperature is calculated based on the equivalent circuit shown in Fig. 5. Liquid cooling is applied to MMC submodule, and the BK CP1426 heatsink from Baknor with

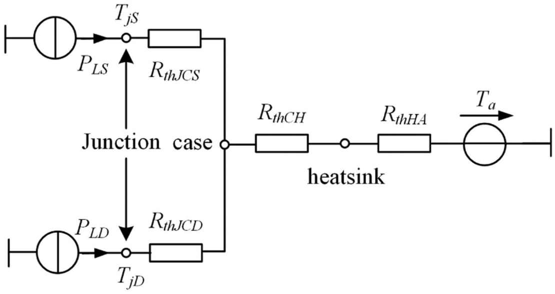

FIGURE 5. **Equivalent thermal model of MMC switches. P_{LS}, P_{LD}, R_{thJCS}, R_{thJCD}, R_{thCH}, R_{thHA}, and T_a represent IGBT losses, diode losses, IGBT junction to case thermal resistance, diode junction to case thermal resistance, case to heatsink thermal resistance, heatsink to ambient thermal resistance, and ambient temperature, respectively.**

TABLE 1. **MMC-SST Detailed Losses at 400 Hz**

MMC losses			50 Hz DRU loss (kW)
switching loss (kW)	conduction loss (kW)	Total loss (kW)	
214	235	449	49.5
Medium frequency DRU loss			SST total loss (kW)
switching loss (kW)	conduction loss (kW)	Total loss (kW)	
50	340	390	888.5

a thermal resistance of 0.006 K/W at 7.5 l/min flow rate is chosen, and the inlet water temperature is assumed as 20°C.

For the medium-frequency diode rectifier, both conduction and turn-off losses need to be considered because of the medium-frequency operating conditions (in our case, it is 400 Hz). The conduction losses calculation method is the same as for the DRU, and the turn-off losses of the diodes are calculated as [24]:

$$P_{RQ} = Q_r \times u_R \times 0.5 \times f \tag{2}$$

where Q_r is the maximum recovery charge given in the datasheet, u_R is the driving voltage after commutation, and f is the operating frequency. Liquid cooling is needed for medium-frequency DRU, and the heatsink of ASENERGI SS15 with a thermal resistance of 0.011 K/W has been chosen.

With the chosen cooling methods, the junction temperatures of the switches of input DRU, MMC, and medium frequency DRU are maintained well within 125°C. The losses are summarized in Table 1.

C. SIZE AND WEIGHT ESTIMATION OF MMC CONVERTER

Since all three topologies have front-side diode rectifiers, their size and weight are not considered in the estimation. As for the secondary side DRU in each topology, these passive switch sizes and weights are not comparable with front side modules. Thus, only the front-side modules size and weight of the three topologies are estimated and calculated.

In Section II-E, the best operating frequency for MMC-SST is observed to be around 400Hz, and the following analysis is for the 400Hz scenario.

For MMC converter module, the size and weight of the 2 kV DC film capacitor are estimated by curve fitting with the data from manufacturer datasheets [29], [30]:

$$size\left(m^3\right) = 9.182 \times C + 4.195 \times 10^{-4} \tag{3}$$

$$weight\,(kg) = 11740 \times C + 16.17 \tag{4}$$

where C represents the value of capacitance in F. As a result, the size and weight estimations of the required 1.45 mF capacitance are 0.014 m^3 and 33 kg, respectively. This formulaic approach facilitates initial comparative assessments across various topologies at a preliminary design stage. Once the optimal topology and operating frequency are established, it is recommended to perform detailed capacitor selection based on component specifications. This step is essential for obtaining precise measurements of component size and weight, which are critical for the practical implementation of the design. The total size and weight of two IGBTs in one module are 1.56×10^{-3} m^3 and 2.4 kg, respectively, calculated directly from the datasheet.

Next, a size estimation of the converter tower is carried out. According to [31], the DC capacitor occupies half the volume of the Alstom Maxsine half-bridge submodule. Based on this observation, adding the size of IGBTs and capacitors and leaving some room for other components, the submodule size is estimated to be 0.04 m^3. Similarly, the submodule weight is estimated to be 50 kg. This estimation serves as a rapid calculation method for comparative stages, while a comprehensive consideration of all component volumes and weights should be done during the final design phase.

The weight value is multiplied by 144 submodules, and the total weight of the submodules is estimated to be 7.2 tons. For MMC converter valve tower size estimation, the insulation requirements need to be considered.

The MMC converter used for MMC-SST is shown in Fig. 6. The arrangement refers to [31]. The insulation designs refer to IEC 60071-1. Only the major parts of the MMC are shown, excluding the conductors, busbars, etc., because this analysis aims to estimate the MMC size considering the insulation distance. The red and blue cylinders represent + and – DC inputs, respectively. The AC outputs are shown in Fig. 6(c). The connection relationship between the modules of one converter tower is shown in Fig. 6(b).

Since the submodule size is estimated as 40 l, and it should be in a cuboid shape, the MMC submodule is estimated to be 0.45 m (length) × 0.3 m (width) × 0.3 m (height).

In the 3D design, four insulation distances, d_1-d_4 have been analyzed. Appendix A has shown the detailed analyzing process. As a result, the total size shown in Fig. 6 is 6.86 m × 3.22 m × 1.95 m = 43 m^3.

A summary of MMC-SST converter size and components weight is shown in Table 2, where other module weight represents an estimation of other components, e.g., gate drivers and protection system.

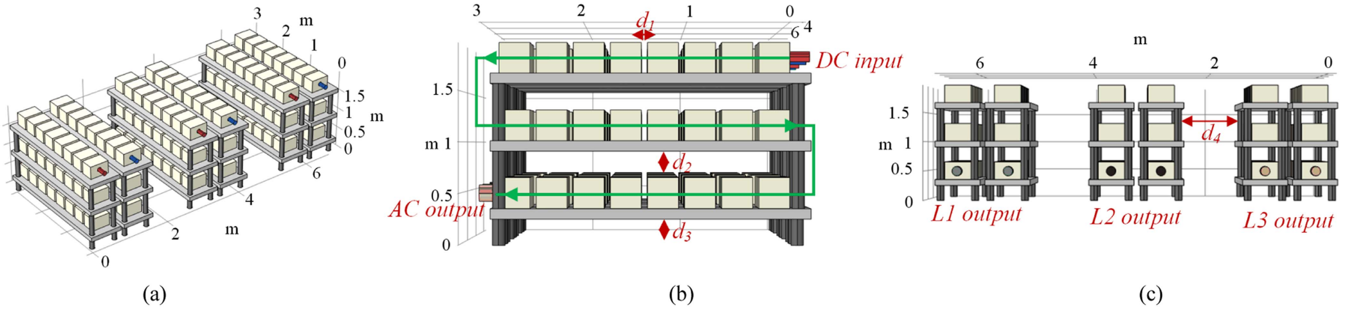

(a) (b) (c)

FIGURE 6. MMC converter 3D modelling (a) overall structure, (b) side view 1, (c) side view 2. In total there are six converter towers, corresponding to 6 arms. Each converter tower has three rows, and each row has eight modules. L1, L2, and L3 represents MMC three phase AC outputs.

TABLE 2. MMC-SST Converter Detailed Size and Weight. The MMC Size Represents the Total Size of the Converter Tower in Fig. 6. The Weight Estimation Focuses on the Capacitor and Switches Weight

MMC size (m^3)	Capacitor weight (ton)	switches weight (ton)	Other Module Weight (ton)
43	4.752	0.3456	2.1

D. DESIGN OF THE MEDIUM-FREQUENCY TRANSFORMER FOR MMC-SST

In order to reduce the MMC harmonics according to IEEE 519, one transformer is configured as Yd, and the other is configured as Dd. The values of the voltages (primary and secondary) and currents are first calculated manually and then verified according to Simulink model. The corresponding primary currents are 580 A for the Yd type and 338 A for the Dd type.

1) YD TRANSFORMER DESIGN

First, the voltage transfer ratio of the transformers is calculated. The MFT primary side line-to-line RMS voltage and the secondary side line-to-line RMS voltage are calculated according to:

$$U_{pri-LL-RMS} = \frac{U_{dc}}{2} \times m \times \sqrt{\frac{3}{2}} \tag{5}$$

$$U_{\sec-LL-RMS} = U_{eletrolyzer} \times \frac{\pi}{3} \times \frac{1}{\sqrt{2}} \tag{6}$$

where m is the MMC modulation index and $U_{electrolyzer}$ is the electrolyzer input voltage. The theoretical voltage transfer ratio of the MFT is calculated as 50. But because of the commutation phenomenon, the selected voltage transfer ratio of the MFT is decreased to 44.5 to reach the required electrolyzer voltage. The number of turns on the secondary side must be selected as low as possible. This is due to efficiency considerations, considering the high current on the secondary side. Practically, it is not feasible to select Ns = 1 as continuously transposed conductors (CTCs) require a minimum length to ensure all strands are appropriately positioned. Therefore,

$$Ns = 2 \rightarrow Np = 52 \tag{7}$$

TABLE 3. Comparison of the Characteristics of Electrical Steel and Amorphous Alloys

Material	Layer thickness (um)	Loss @400 Hz (W/kg)	B_{sat} (T)	Permeability	Density (kg/m^3)
Grain-oriented electrical steel	100	16	2	2000	7800
Amorphous	25	1.3	1.63	6500	7300

where Ns is the number of secondary turns, and Np is the number of primary turns. The primary line-to-line voltage is $U_{pri\text{-}LL\text{-}RMS} = 25429$ V, and the phase voltage of the primary RMS value is $U_{pri\text{-}ph\text{-}RMS} = 14615$ V.

The following is a brief explanation of core material selection and design. The cross-section of the core can be calculated as follows:

$$A_c = \frac{U_{pri-ph-RMS}}{k_c \times k_w \times B_m \times f \times N_p} \tag{8}$$

where k_c is the core stacking factor, k_w is the form factor, B_m is the maximum flux density in the core, and f is the frequency.

Different core materials are feasible. For high-power applications, grain-oriented electrical steel and amorphous are more common choices [2]. The characteristics of electrical steel and amorphous are compared in Table 3. According to Table 3, electrical steel is a good choice for 50/60 Hz applications. However, the higher the frequency, the higher the core loss. Therefore, alternative materials such as amorphous are more beneficial.

Another difference between a transformer made of electrical steel and the one made of amorphous is that electrical steel transformers are made of several plates for the limbs and yokes. However, amorphous transformers are made by a number of thin strips which are placed next to each other to form the entire core. From a manufacturing point of view, to insert the coils into an electrical steel core, the manufacturer removes the upper yoke, inserts the coils, and puts the upper yoke again [32], [33]. For an amorphous core, the manufacturer unlaces the strips, inserts the coils, and re-laces the strips again [12]. Although the manufacturing procedure is more complex for the amorphous-based transformers, amorphous

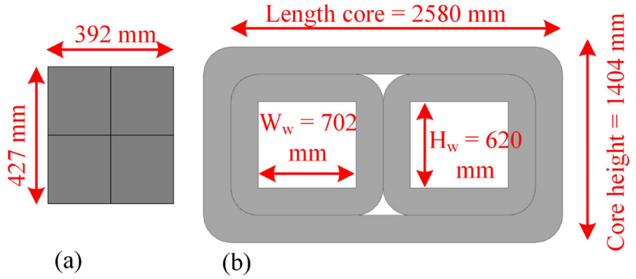

FIGURE 7. Details of the core design for the MMC-SST transformer: (a) the cross-section of the core, (b) the 3D view of the magnetic core.

is selected as the magnetic material of the core since the frequency in the present application is relatively high. The selected alloy is Metglas 2605HB1M, which is available in strips with various widths, such as 142.2 mm, 170.2 mm, and 213.4 mm [34]. The nominal thickness of the strips is 25 μm, which results in a good lamination.

Assuming $B_m = 1.2$ T, $k_c = 0.79$, $k_w = 4.44$, and $f = 400$ Hz in (8) results in $A_c = 0.167$ m^2. For MMC-SST topology, amorphous strips with a width of 213.4 mm are selected. Therefore, the width of the core is calculated as 392 mm, as shown in Fig. 7(a). The core is made of two cores stacked on top of each other. The core dimensions are shown in Fig. 7(b).

The core loss of the transformer is calculated as follows [35]:

$$P_c = Volume_c \times \varrho_c \times P_{c0} \times \left(\frac{f}{f_0}\right)^{\alpha} \times \left(\frac{B_m}{B_{m0}}\right)^{\beta} \times \left(\frac{k_w}{k_{w0}}\right)^{2(\alpha-1)} \tag{9}$$

where $Volume_c$ is the volume of the core, ϱ_c is the density of the core, P_{c0} is the loss of the core per kg regarding Table 3, f_0 is the reference frequency (400 Hz), B_{m0} is the reference maximum flux density (1.0 T), k_{w0} is the reference form factor (4.44), α=1.47 is the frequency dependency, and β=1.52 is flux density dependency.

Besides core losses, transformers are affected by "stray losses", which stem from eddy currents induced in the transformer's conductive components, such as clamps, flitch plates, tanks, and shunts [36]. The calculation of stray losses is a complex task, requiring the utilization of Finite Element Method (FEM) simulations or experimental estimation techniques to obtain accurate measurements [37], [38]. In this paper, stray loss is estimated based on the method described in [39].

After the core design is accomplished, the CTCs are selected for the conductors of the transformer. CTCs have two advantages. Firstly, CTCs can mitigate the skin effect due to the presence of several strands. Secondly, with the transposition of the strands, they all have similar lengths and experience similar background magnetic fields to avoid circulating current in the windings [40]. The primary CTC size CTC_{pri} and secondary CTC size CTC_{sec} can be designed as follows:

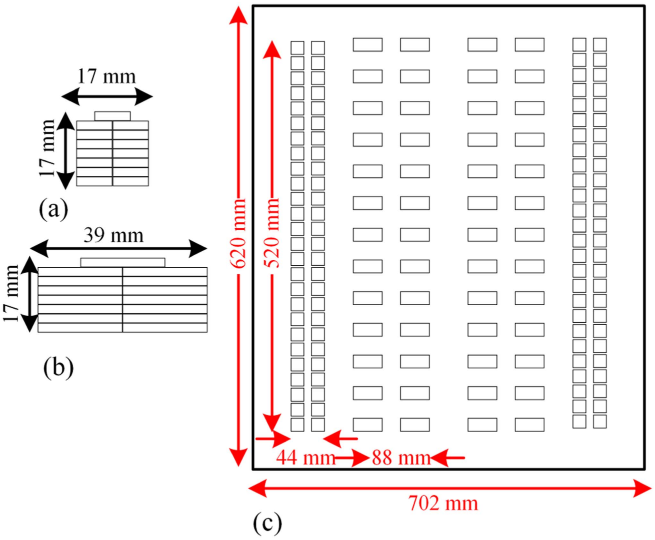

FIGURE 8. The details of the winding design of the MMC-SST transformer: (a) Yd CTC of primary, (b) Yd CTC of secondary, (c) Yd window.

$$A_p = \frac{I_{pri-ph-RMS}}{J_p} = \frac{580}{2.5} = 232mm^2$$

$$\rightarrow CTC_{pri} : 15 \times 8 \times 2mm^2 (n \times w \times t) \tag{10}$$

$$A_s = \frac{I_{\sec-ph-RMS}}{J_s} = \frac{15200}{2} = 7600mm^2$$

$$\rightarrow CTC_{sec} : 13 \times 15 \times 19 \times 2mm^2 (N \times n \times w \times t) \tag{11}$$

where A_p and A_s are required primary and secondary conductor size, respectively, $I_{pri\text{-}ph\text{-}RMS}$ and $I_{sec\text{-}ph\text{-}RMS}$ are phase current RMS values of the primary and secondary, respectively, J_p and J_s are the current density of the primary and secondary, respectively, N is the number of parallel paths on the secondary side to handle huge amounts of current, n is the number of strands (which is an odd number), w is the width of each strand, and t is the thickness of each strand.

The primary and secondary conductors are shown in Fig. 8(a) and (b), respectively. The transformer window is designed as shown in Fig. 8(c). Note that because of high-current busbars, the secondary is built over the primary. The primary is made of 26 disks, and each has two turns. The secondary is made of 13 parallel disks to handle the high-current. While the distance between disks in the primary is for the oil ducts, the secondary has more space between disks to provide access to the busbar connection.

A FEM simulation using a 3D ANSYS Maxwell model was performed to determine the leakage and magnetizing inductances, crucial for voltage impedance calculations and the resonant topology designs discussed in Sections III and IV. Additionally, a 2D COMSOL model was used to compute the AC load losses, a key factor in assessing transformer efficiency and informing cooling system design. The results

TABLE 4. FEM Results for MMC-SST

Configuration	Parameter	Value
Yd	L_{lk}	1.399 mH
	r_p	816.12 μΩ/m
	r_s	50.356 μΩ/m
Dd	L_{lk}	4.001 mH
	r_p	1549.8 μΩ/m
	r_s	51.455 μΩ/m

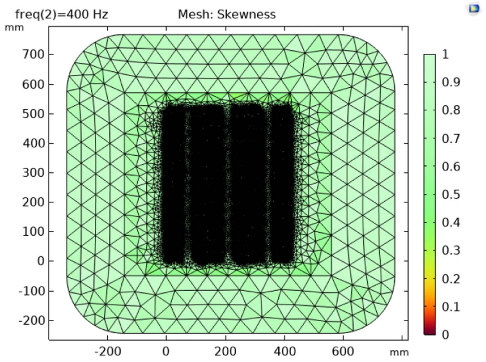

FIGURE 9. Meshing performance of the COMSOL 2D simulation for Yd MMC-SST MFT.

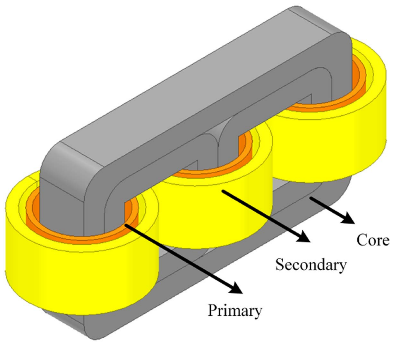

FIGURE 10. 3D view of the MMC-SST MFT.

of the FEM simulations for MMC-SST MFT are summarized in Table 4. The meshing performance of the FEM simulation is shown in Fig. 9. The 3D view of the MMC-SST MFT in ANSYS Maxwell is shown in Fig. 10.

To estimate the copper loss of the transformer, first the Mean Length per Turn (MLT) is calculated as follows:

$$MLT_p = \pi \times (D_p + W_p) \tag{12}$$

where D_p is the diameter and W_p is the width of the primary winding. Then, the length of the primary can be calculated as follows:

$$l_p = MLT_p \times N_p \tag{13}$$

According to the FEM simulation result in Table 4, the average AC resistance r_p is 816.12 $\mu\Omega$/m. The load loss based on the AC resistance can be calculated as follows:

$$R_p = l_p \times r_p \tag{14}$$

TABLE 5. Temperature Rise Limits According to IEC 60076-2 [41]

Components	Temperature rise limit (K)
Top insulation liquid	60
ON (Oil-Natural) and OF (Oil-Forced) cooling systems – average winding	65
Hot-spot winding	78

TABLE 6. MMC MFT Detailed Losses. The Copper Loss is Calculated Based on (15), and the Core Loss is Calculated Based on (9)

Copper loss (kW)	Core loss (kW)	Stray loss (kW)	Total losses (kW)
630.1	26.2	39.3	695.6

TABLE 7. MMC MFT Detailed Size and Weight

Transformer size (m^3)	Copper weight (ton)	Core weight (ton)	tank weight (ton)	Oil weight (ton)
15.6	3.85	16.79	1.52	5.45

$$Loss_p = 3 \times R_p \times I^2_{pri-ph-RMS} \tag{15}$$

The weight of the primary winding can be calculated as follows:

$$Weight_p = 3 \times l_p \times CTC_{pri} \times \varrho_{cu} \tag{16}$$

where ϱ_{cu} is the density of copper. The loss and weight of the secondary winding can be calculated using a similar method. Tables 6 and 7 in Section II-D-4 summarize the loss and weight for the MFTs.

2) DD TRANSFORMER DESIGN

The design of the transformer for the Dd configuration is similar to the design of the Yd transformer. The difference is in the primary voltage, and in this case, it is $U_{pri\text{-}LL\text{-}RMS} = U_{pri\text{-}ph\text{-}RMS} = 25429$ V. To maintain the same voltage on the secondary side, the number of turns on the primary side is higher (90 turns compared to 52 turns). Accordingly, the primary current RMS value is 338 A. Therefore, the primary CTC can be designed as $CTC_{pri} = n{\times}w{\times}t = 13 \times 5 \times 2 = 130$ mm^2. The primary consists of 30 disks, which have 3 turns each. The secondary structure is the same as Yd transformer. The AC resistances per unit length for Dd transformer are $\mathrm{r_p} = 1549.8$ $\mu\Omega$/m and $\mathrm{r_s} = 51.544$ $\mu\Omega$/m, as summarized in Table 4.

3) INSULATION CONSIDERATIONS, THERMAL MANAGEMENT, AND TANK DESIGN

Because of the power rating and the amount of loss of the transformers, the MFT in the present study is oil-type, which is filled with mineral oil. The temperature rise limits according to IEC 60076-2 [41] are summarized in Table 5. Therefore, the oil temperature for the loss calculations in the COMSOL 2D simulation is considered as $T_{oil} = 78 + T_{amb}$, where T_{amb} is the ambient temperature. The MFT for MMC-SST topology consists of two active parts, a Yd and a Dd transformers, in

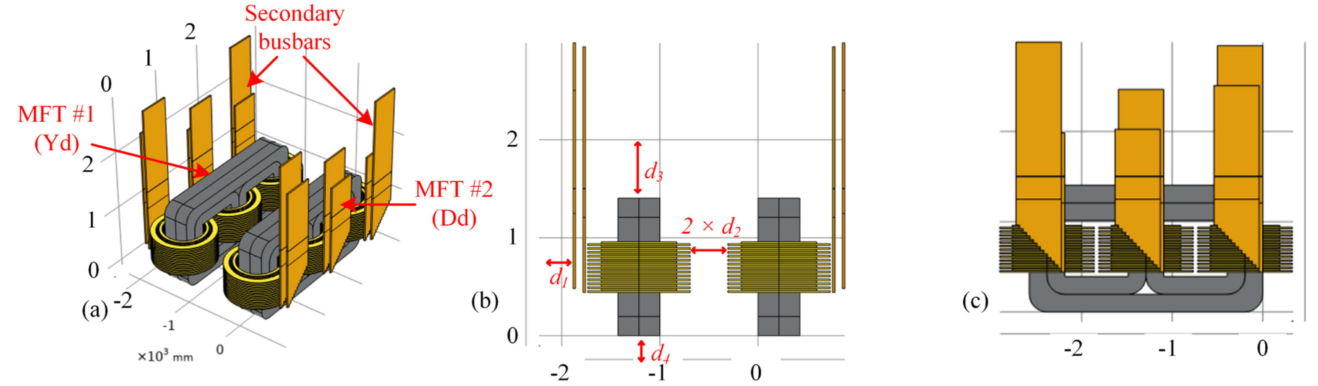

FIGURE 11. 3D view of the active parts inside the tank (a) overall view, (b) side view 1, and (c) side view 2. The high-current busbars on the secondary side are designed to facilitate the parallel connection of the secondary disks and provide sufficient space for the horizontal busbars outside the tank.

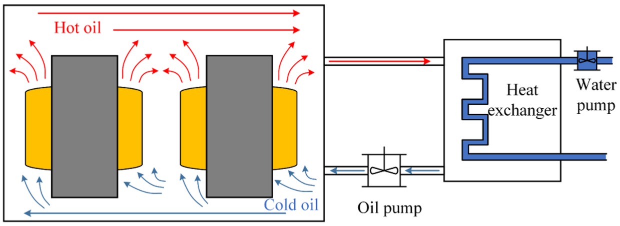

FIGURE 12. Schematic of an oil-forced, water-forced (OFWF) cooling system.

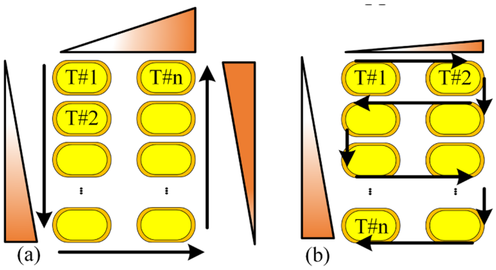

FIGURE 13. Comparison of voltage distribution of (a) a layer winding and (b) a disk winding. T#1, T#2, and T#n represent the 1st turn, 2nd turn, and nth turn, respectively.

one tank. The cooling system is oil-forced and water-forced (OFWF), as shown in Fig. 12.

To avoid complexity, it is assumed that the oil flow inside the tank has no eddy patterns. The oil flow between disks is assumed to be laminar. The thermal design follows the methods described in [42], [43], [44]. The active parts inside the tank are shown in Fig. 11 . As shown in Fig. 11, there are distances between MFTs and the side wall of the tank (d_1), two MFTs (d_2), MFTs and upper lid of the tank (d_3), and MFTs and bottom of the tank (d_4). More information about the insulation thermal design in addition to the details of FEM-based simulations are available in Appendix B.

The CTC strands are enameled, and the CTC itself is insulated by oil-immersed paper. A pressboard makes the disk structure support the winding structure during normal operation and fault forces. The windings are made of disks, which are more compact and provide better voltage distribution, as shown in Fig. 13.

The rated voltage of the transformer is calculated using (5) which is 25.429 kV$_{\text{rms}}$. For insulation design, the input voltage is considered $U_{pri\text{-}LL\text{-}RMS} = 25.5$ kV. Based on the IEC 60076-3, the test voltage levels for the transformers with the highest voltage for the equipment winding between 24 kV and 36 kV are as follows: Full Wave Lighting Impulse (LI) = 170 kV, Chopped Wave Lighting Impulse (LIC) = 187 kV, and Line Terminal AC Withstand (LTAC) = 70 kV [45]. However, for the present design, the Lightening Impulse test is not considered because there is no risk of lightening in this system for two reasons. Firstly, the MFT is not connected to an exposed transmission line. Secondly, there are front-end components like autotransformer, DRUs, and MMC before the transformer, which are protected against the lightning. Therefore, MFT is designed to handle the Terminal AC Withstand (LTAC) test which is 70 kV$_{\text{rms}}$. The cores and the tank are earthed, thus they have zero potential. Because of the presence of high-current busbars of the low voltage winding, the primary winding which is connected to MV is placed near the core, and the secondary winding is placed over the primary. This means the highest electric field is between the primary and core, especially near the edges of the core.

4) OVERALL METRICS OF THE MMC-SST MFT

The transformers dimensions are 3232 × 1044 × 1404 mm ($x \times y \times z$). Thus, the volume of active parts is 9.48 m^3. The thickness of the tank plates is selected as $t_{tank} = 5$ mm. Thus, the tank size is calculated as:

$$X_{\text{tank}} = x_{trans} + (2 \times d_1) + (2 \times t_{\text{tank}}) \tag{17}$$

$$Y_{\text{tank}} = (2 \times d_1) + (2 \times d_2) + (2 \times y_{trans}) + (2 \times t_{\text{tank}}) \tag{18}$$

$$Z_{\text{tank}} = d_3 + d_4 + z_{trans} + (2 \times t_{\text{tank}}) \tag{19}$$

TABLE 8. Total Loss, Size, and Weight of SST. Power Converter Loss Includes Front Side Dru Loss, MMC/ISOP Loss, and Medium Frequency Dru Loss. Converter Size Represents the Converter Tower Size Considering insulations. The Transformer Size Represents the Total Size of the Tank. The Transformer Weight Includes Active Parts Weight, Tank Weight, and Oil Weight

Topologies	Power converter loss (kW)	Transformer Loss (kW)	Converter size (m^3)	Transformer size (m^3)	Chiller size (m^3)	Converter weight (ton)	Transformer weight (ton)	Chiller weigl (ton)
MMC-SST (400Hz)	888.5	695.6	43	15.6	78	7.2	27.6	14.6
MMR (1000Hz)	751.5	817	39.9	10.44	77.45	5.76	16.35	14.5
ISOP (1000Hz)	481.5	806.3	8.94	13.78	64.24	2.4	28.8	11.98

where X_{trans}, Y_{trans}, and Z_{trans} represent transformer dimensions and clearances ($d_1 - d_4$) are as shown in Fig. 11 and explained in Appendix B. Therefore, the volume of the tank is calculated as follows:

$$\begin{aligned} V_{\text{tank}} &= X_{\text{tank}} \times Y_{\text{tank}} \times Z_{\text{tank}} \\ &= 3.442 \times 2.498 \times 1.814 = 15.6m^2 \end{aligned} \tag{20}$$

The weight of the tank and the transformer oil are 1521 kg and 5447 kg, respectively.

As a result, the detailed loss, total size, and weight breakdown of MFTs are shown in Tables 6 and 7.

The total size, weight, and loss of the transformers are summarized in Table 8. In addition, the loss, size, and weight of power converter parts are also shown. Besides the size and weight information of power converter and MFTs, the chiller's information is also presented.

To cool down the cooling liquid used in the heatsink and the medium frequency transformer, a chiller is needed. The chiller size and weight are considerable and need to be added. According to the product data from DeltaTemp [46], it is possible to derive curve-fitting models that correlate size and weight with cooling capacity. Curve-fitting expressions can be formulated as follows:

$$chillersize(m^3) = 4.7e - 5 \times P(W) + 6.015 \tag{21}$$

$$chillerweight\ (kg) = 8.974e - 3 \times P(W) + 870.4 \tag{22}$$

The total power loss P requiring liquid cooling amounts to 1534.6 kW, comprising 839 kW from converter loss (MMC and secondary DRU) and 695.6 kW from MFT loss. Thus, the required chiller cooling capacity is 1534.6 kW, and its corresponding size and weight are estimated to be 78 m^3 and 14.6 tons, respectively.

E. PERFORMANCE METRICS AT DIFFERENT FREQUENCIES

Following a similar design process as shown above, the losses, sizes, and weights at different frequencies of the MMC-SST topologies are shown in Fig. 15(a). In the comparative analysis of frequency response, note that for the transformer, only active parts (core and windings) are considered since this simplification is used to ensure manageable computations. For a similar reason, though the converter tower will be different for each analyzed frequency, most of the size changes come from the capacitor size differences between frequencies. Thus, only the capacitors are included to represent the dimensions of the converter parts.

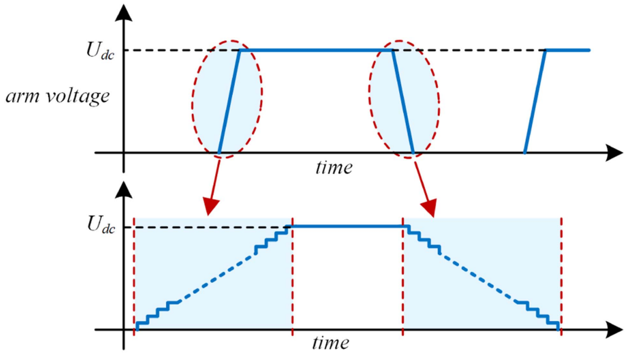

FIGURE 14. Quasi Square Wave modulation method. U_{dc} represents the input DC voltage. The generated staircase waveforms are designed to emulate those from two-level soft-switching converters, ensuring that the operating principles of the MMR align with those of the two-level, soft-switching LLC converters.

As depicted in Fig. 15(a), the optimal frequency for the MMC-SST varies with respect to loss, weight, and size. The primary objective of using SST is to reduce the size and weight compared to traditional line frequency transformer-based converter topologies. This reduction is particularly advantageous in high-power applications, as it minimizes the physical footprint of installations where land and space usage can be costly. Therefore, in our optimal design considerations, size and weight are prioritized over losses. Consequently, the most suitable operating frequency for the MMC-SST has been identified as approximately 400 Hz. At this frequency, the design achieves the smallest size and very low weight while maintaining relatively low losses.

III. PERFORMANCE METRICS FOR MODULAR MULTI-LEVEL RESONANT BASED SOLID-STATE TRANSFORMER

A. LOSS, SIZE, AND WEIGHT ESTIMATION OF THE POWER CONVERTERS

As mentioned in the introduction, the differences between MMR and MMC are inserted resonant capacitors and modulation methods. The Quasi Square Wave modulation method for the MMR is depicted in Fig. 14. The complete MMR model, constructed in Simulink, showcases key waveforms in Fig. 17, with Fig. 17(a) specifically illustrating the resulting arm voltages.

In theory, for MMR, primary side switches can achieve ZVS, and secondary side diodes can achieve ZCS, but because

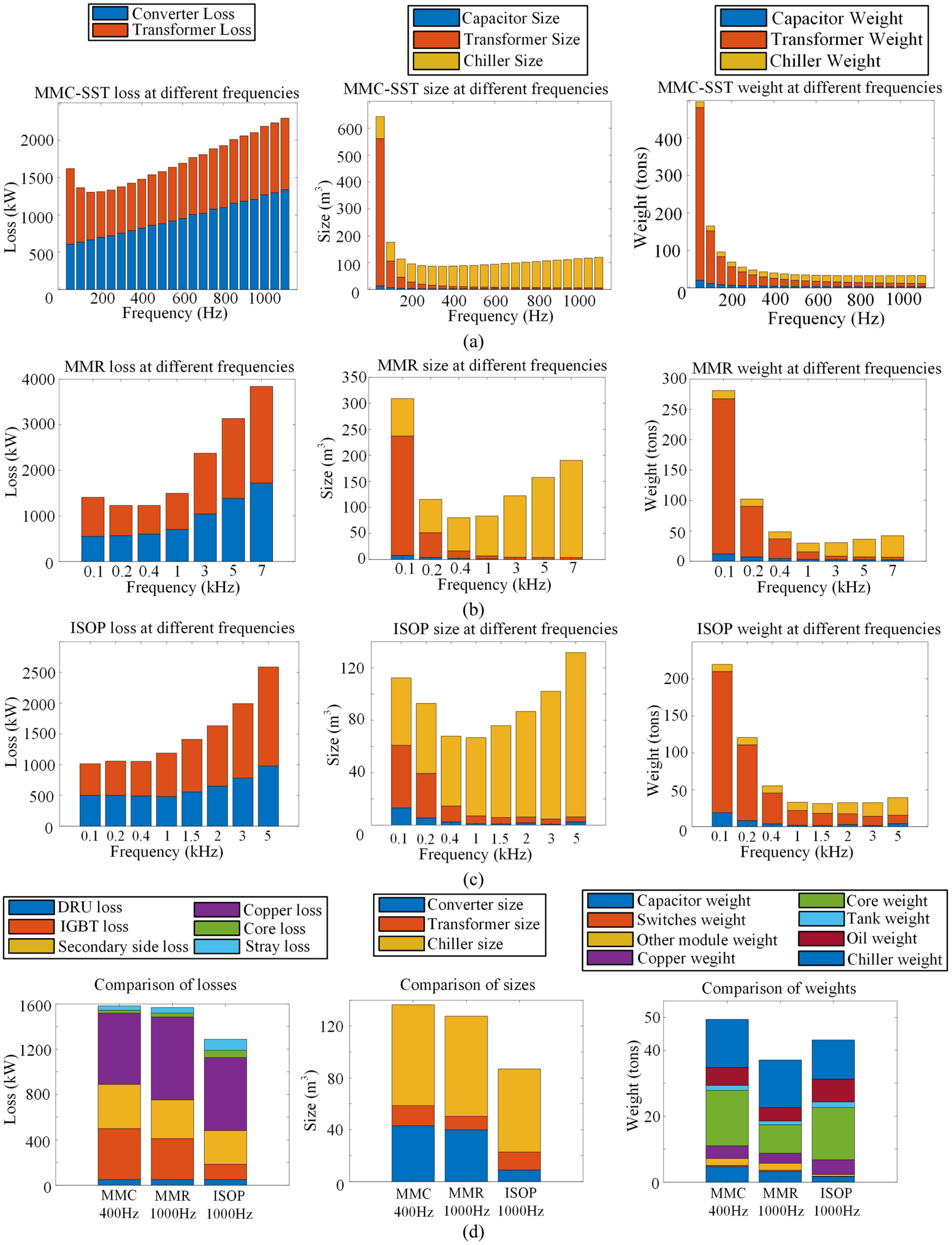

FIGURE 15. (a) MMC-SST (b) MMR (c) ISOP loss, size, and weight at different frequencies. In these figures, for transformer loss, size, and weight estimations, only the active parts are considered for simplicity. For the converter section, the focus is on the changes in size and weight of the capacitor, which are influenced by variations in frequency. Changes in other components are considered minimal and thus not accounted for in this analysis. (d) Topologies comparison results. The optimal operating frequencies for the MMC-SST, MMR, and ISOP are 400 Hz, 1000 Hz, and 1000 Hz, according to (a), (b), and (c).

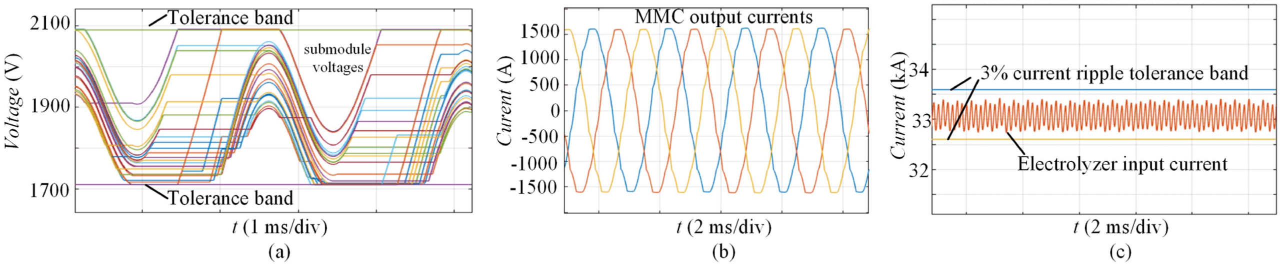

FIGURE 16. Key waveforms of the MMC-SST: (a) submodule voltages of phase A upper arm, balanced by the cell tolerance band (CTB) method, (b) MMC output currents, and (c) electrolyzer input currents maintained within a 3% current ripple band.

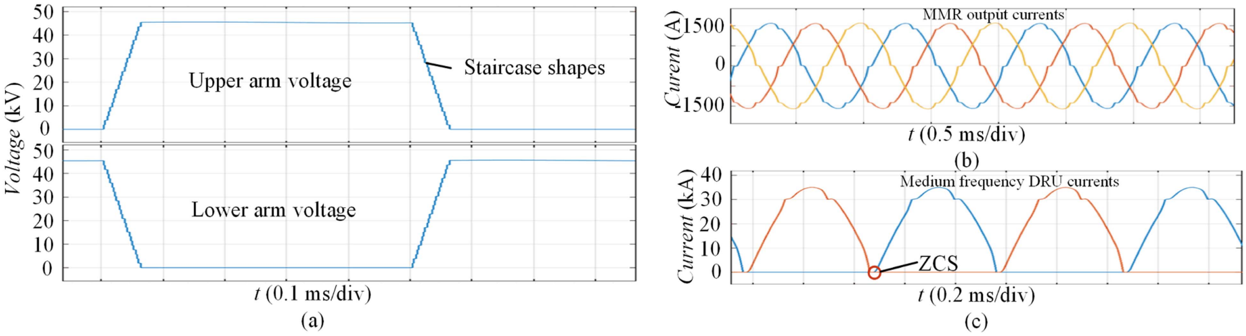

FIGURE 17. Key waveforms of the MMR: (a) phase A upper and lower arm voltages displaying staircase edges, according to the modulation method in Fig. 14, (b) MMC output currents with low THD, and (c) medium frequency DRU current exhibiting zero current switching. Additionally, the submodule voltages are balanced similarly to Fig. 16(a), and the electrolyzer input currents are maintained within a 3% current ripple band, as shown in Fig. 16(c).

of the MMC arm current DC bias, the switching losses will exist, as witnessed in the following loss analysis.

The overall configuration of the MMR with the secondary side DRUs is shown in Fig. 2. In contrast to the MMC-SST, which employs a YdDd medium frequency transformer configuration to mitigate MMC output current harmonics and associated module losses, the MMR adopts a DdDd configuration. This shift is primarily due to the theoretical expectation that resonant and total MMC output currents in the MMR are sinusoidal, eliminating the necessity for a twelve-pulse configuration. Moreover, manufacturing simplicity is achieved as both medium-frequency transformers share the same configuration. Ideally, a YdYd transformer configuration would be preferable for high input voltage to low output voltage applications. However, according to [47], the resonant current in a three-phase Yd resonant converter is not sinusoidal and contains significant harmonics, adversely affecting MMC loss reduction. According to simulations, the DdDd configuration ensures minimal THD in resonant currents, thus making it the preferred choice for reducing MMC losses.

The resonant passive components design methods are referred to two-level LLC converters [48]. The transformer designs will be different from the MMC-SST transformers. Dd transformer turn ratio n_1 is calculated as [49]:

$$n_1 = \frac{U_{dc}}{U_{electrolyzer}} \tag{23}$$

where $U_{electrolyzer}$ represents electrolyzer rated input voltage. The turn ratio is tuned slightly considering output voltage safety room, and the resulting turn ratio of Dd transformer is 52. The parameters of the MMR modules remain the same as those of MMC-SST, e.g., submodule capacitance, number of submodules, etc.

For the power converter loss estimation, the front side twelve pulse DRU losses remain the same as MMC-SST. However, for MMC in MMR, the switching losses will be different because of the soft switching mechanism, and the conduction losses are also different because of different current waveforms. The following theoretically calculate the losses of MMR. For Dd transformer, secondary side current and voltage peak values can be calculated as:

$$U_{\sec-ph-peak} = U_{\sec-LL-peak} = \frac{\pi}{3} \times U_{eletroylzer} \tag{24}$$

$$I_{\sec-line-peak} = \sqrt{3} \times I_{\sec-ph-peak} = \frac{\sqrt{3} \times P_{total} \times 2}{U_{\sec-ph-peak} \times 3} \tag{25}$$

The primary side voltage and current are calculated as:

$$U_{pri-ph-peak} = U_{\sec-ph-peak} \times n_1 \tag{26}$$

$$I_{pri-line-peak} = \sqrt{3} \times I_{pri-ph-peak} = \frac{\sqrt{3} \times P_{total} \times 2}{U_{pri-ph-peak} \times 3} \tag{27}$$

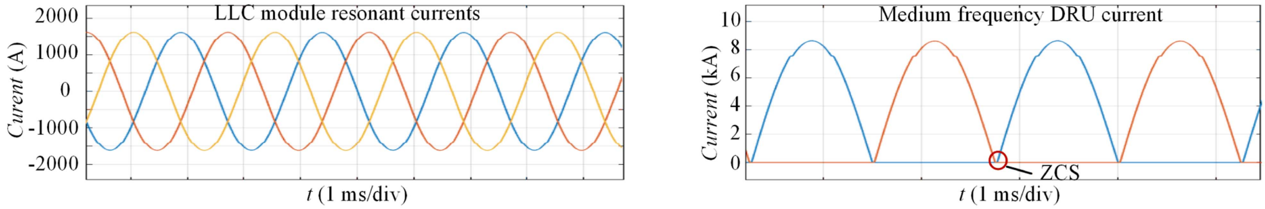

(a)

(b)

FIGURE 18. Key waveforms of the ISOP for one LLC submodule: (a) three-phase resonant currents displaying a highly sinusoidal shape, and (b) medium frequency DRU current demonstrating zero current switching. Additionally, the electrolyzer input currents are consistently maintained within a 3% current ripple band, similar to that depicted in Fig. 16(c).

As a result, the primary side line current peak value is calculated as 702 A. The total output current of MMC is:

$$I_{total} = 1404\cos(\omega t + \varphi_1) \tag{28}$$

At the resonant frequency, the LLC resonant circuit is inductive, thus, the MMC output current phase angle should be slightly behind the output square voltage. With a suitable design, the delay angles will not be far from 0°, as seen from the literature [19]. For the convenience of theoretical loss analysis, MMC phase current is assumed to be:

$$I_{total} = 1404\cos(\omega t) \tag{29}$$

Thus, the current is in phase with the MMC output square waves. The upper and lower arm currents of phase A are:

$$i_p = \frac{I_{dc}}{3} + \frac{I_{total}}{2} = 328 + 702\cos(\omega t) \tag{30}$$

$$i_n = \frac{I_{dc}}{3} - \frac{I_{total}}{2} = 328 - 702\cos(\omega t) \tag{31}$$

The key waveforms and corresponding primary side notations of the circuits are shown in Figs. 19 and 20, and for simplicity, only one phase is shown.

As seen from Fig. 20, the currents are symmetrical for the upper and lower arms, so only the upper arm losses are calculated, and the losses are multiplied by the number of arms. Since the current expressions for the upper and lower arms have been derived above, the conduction losses can be calculated using the same method as MMC-SST.

As for switching losses, for i_{1a} and i_{1b}, six circles have been marked on the waveforms for the switching instances. Because of the DC current bias, switching losses will occur compared with a normal two-level resonant converter. The following analyses these 6 switching instances. For i_{1b}, the current completely goes through the IGBT of S_{1b}. At instance 1, the IGBT turns on with non-ZVS, and at instance 2, the IGBT turns off with non-ZCS. For i_{1a}, at instance 3, the diode of S_{1a} turns on, however, the turn-on losses of the diodes are usually omitted. At instance 4, the diode of S_{1a} turns off, and the IGBT of S_{1a} turns on with ZVS. At instance 5, the IGBT of S_{1a} turns off with ZCS, and the diode of S_{1a} turns on. At instance 6, the diode of S_{1a} turns off with reverse recovery losses. The current values can be calculated at each instance, and the turn-on, turn-off, and reverse recovery energies can be referred to in the datasheet. The switching losses are computed by those energy losses multiplied by the switching frequency.

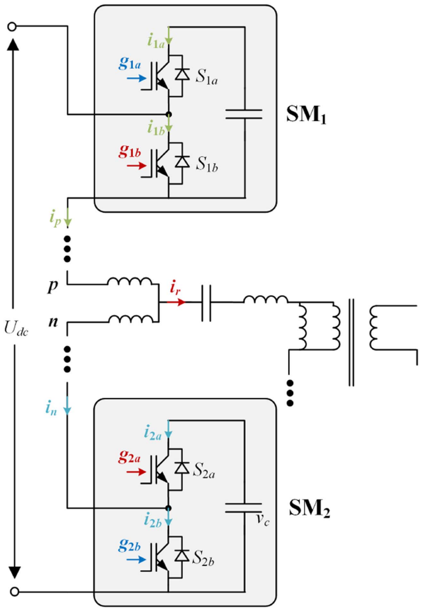

FIGURE 19. MMR primary side notations. For simplicity, only one submodule in each arm for one phase is shown. S_{1a} and S_{1b} denote the upper and lower IGBT modules of SM$_1$, respectively, while g_{1a} and g_{1b} correspond to their gate signals. S_{2a}, S_{2b}, g_{2a}, and g_{2b} are similarly defined for SM$_2$. i_p, i_n, and i_r refer to the upper arm, lower arm, and resonant currents, respectively.

As for the secondary side DRU, because of the working principle of the resonant converter, there is no reverse recovery of the diodes, thus, only the conduction losses of the diodes are considered. Because the primary side resonant current is pure sinusoidal at the resonant frequency, and the magnetizing inductance is much higher than the leakage inductance of the MFT, the secondary side current is also assumed to be sinusoidal. The conduction losses calculation method of the secondary side DRU is the same as that of MMC-SST. As a result, the conduction losses, switching losses of MMC, and the conduction losses of secondary side DRU are 191 kW, 68 kW, and 341 kW, respectively, for 400 Hz. For 1000 Hz, only the switching losses of the MMC will change to 170 kW, and others will remain unchanged.

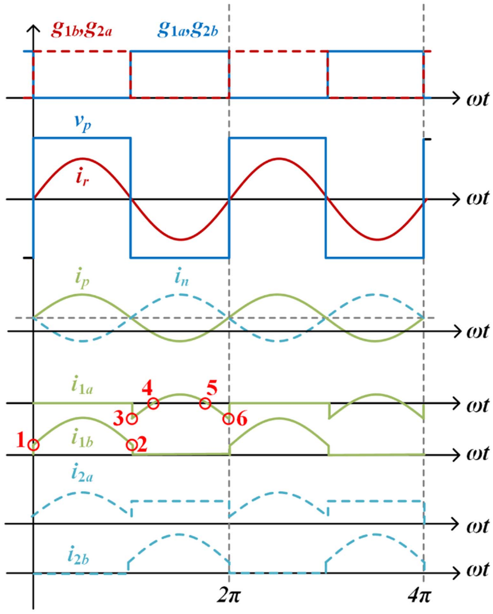

FIGURE 20. Key waveforms of the primary side converter corresponding to Fig. 19. Six switching instances are marked consecutively for upper arm submodule for theoretical loss analysis and calculation.

TABLE 9. MMR Converter Detailed Losses

DRU loss (kW)	MMC loss (kW)	Secondary side DRU loss (kW)	Total loss (kW)
49.5	361	341	751.5

As a result, a summary of the losses of different components at 1000 Hz is shown in Table 9.

Fig. 17(b) displays the simulated MMR output currents, which deviate slightly from a perfect sinusoidal shape due to the delay angle introduced by the Quasi Square Wave modulation. Fig. 17(c) presents the medium frequency DRU current, clearly exhibiting ZCS characteristics. The model's behavior aligns closely with theoretical analysis.

The following size and weight estimations are based on 1000 Hz operating frequency, as the next section shows that the best frequency for MMR is 1000 Hz. Submodule capacitance installed in the 1000 Hz MMC is estimated as 1.45 mF×400/1000=0.58 mF, where 1.45 mF is the capacitance value used in 400 Hz MMC-SST. The capacitor size and weight for 0.58 mF MMC are estimated as 6×10^{-3} m^3 and 23 kg, based on (3) (4). The switches' size and weight remain unchanged, at 1.56 $\times10^{-3}$ m^3 and 2.4 kg. Assuming the weight and volume of other module components remain the same as the 400 Hz MMC submodule, the submodule size is 0.031 m^3, and the submodule weight is 40 kg. The total submodule weight of MMC converter is 5.76 tons. The submodule block dimensions are assumed to be 0.35 m (length) × 0.3 m (width) × 0.3 m (height). The insulation design is similar to the MMC-SST, and the 3D modelling will not be repeated here for simplicity. The insulation distances d_1, d_2, d_3, and d_4 defined in Section II-C are the same as MMC-SST. But because of smaller submodules, the total size will be different from MMC-SST, and the total size of MMR converter is 6.29 m × 3.22 m × 1.97 m = 39.9 m^3. Table 10 shows a summary of the MMR converter's size and components weight.

TABLE 10. MMR Converter Detailed Size and Weight

MMC size (m^3)	Capacitor weight (ton)	switches weight (ton)	Other Module Weight (ton)
39.9	3.312	0.3456	2.1

TABLE 11. FEM Results for MMR MFTs

Frequency	Configuration	Parameter	Value
1000	Dd	L_{lk}	3.762 mH
		r_p	2970.4 μΩ/m
		r_s	71.761 μΩ/m

TABLE 12. MMR MFT Detailed Losses

Copper loss (kW)	Core loss (kW)	Stray loss (kW)	Total losses (kW)
733.5	33.5	50.25	817

TABLE 13. MMR MFT Detailed Size and Weight

Transformer size (m^3)	Copper weight (ton)	Core weight (ton)	tank weight (ton)	Oil weight (ton)
10.44	3.04	8.6	1.15	4.04

B. DESIGN OF THE MEDIUM FREQUENCY TRANSFORMER FOR MMR

The MMR topology has two Dd MFTs. The voltage and current of the transformers are measured in the Simulink model.

For the Dd transformer of MMR topology, $\int U_{pri-ph}dt = 9.28$, $N_p = 104$, and $N_s = 2$. The remaining design process is similar to the MFTs in MMC-SST, which will not be repeated here.

The physical structure of MMR MFT is similar to MMC-SST MFT, where there are also two active parts inside one tank, and rating power and voltages are similar.

The FEM simulation results of MMR MFT are summarized in Table 11.

The MFT detailed loss is summarized in Table 12, and the size and weight breakdown information is summarized in Table 13.

The loss, size, and weight information for power converter, MFTs, and chiller for MMR at 1000 Hz are summarized in Table 8.

C. PERFORMANCE METRICS AT DIFFERENT FREQUENCIES

Following a similar analysis process, the losses, sizes, and weights at different frequencies of the MMR topologies are shown in Fig. 15(b). As shown in Fig. 15(b), the optimal fundamental frequency for the MMR topology is identified as approximately 1000 Hz, prioritizing size and weight reduction as key design targets.

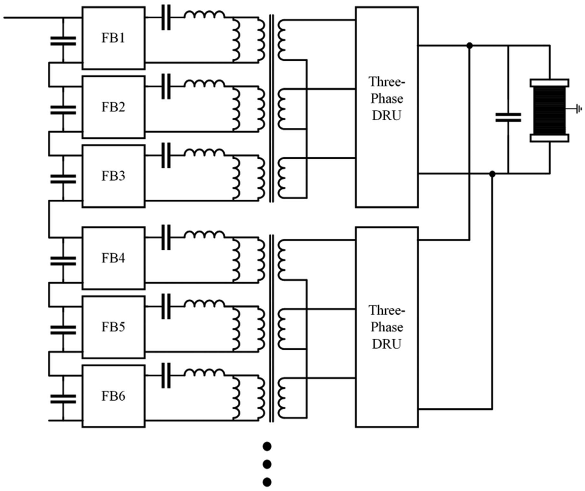

FIGURE 21. Three-phase ISOP system. Three-phase LLC submodules are connected together to form an ISOP configuration. The primary side of these three submodules is shifted with a 120° phase delay. FB represents full bridge modules.

The frequency sweep range for MMR is different from MMC-SST as shown in Fig. 15(a), because the analysis aims to identify the optimal frequency corresponding to the turning point. Due to the soft switching characteristics of MMR, it is necessary to consider a broader frequency range. This approach ensures that the optimal frequency is accurately determined. A similar rationale applies to the frequency sweep range analysis for the ISOP topology.

IV. PERFORMANCE METRICS FOR INPUT SERIES OUTPUT PARALLEL SOLID-STATE TRANSFORMER

A. LOSS, SIZE, AND WEIGHT ESTIMATION OF THE POWER CONVERTERS

As discussed in the introduction, LLC is more suitable than DAB for this unidirectional application scenario. At the initial stage of the design, the single-phase LLC was chosen as the sub-module for the ISOP. Although this topology offers better scalability, it has notable disadvantages. Firstly, single-phase transformers are heavier and larger compared to three-phase transformers with the same voltage level and capacity. Secondly, the output capacitance is large due to the intrinsic second-order power ripple present in single-phase systems.

An alternative topology is shown in Fig. 21. Full bridge inverters are used because of the high-power requirement of modules. The voltage rating of the switches remains the same as the MMC-SST, i.e., 3.3 kV IGBT with a derated safety voltage of 2 kV. The number of cascaded full bridges is $N = ceil(U_{dc}/U_{IBGT_{derated}})$=24.

Instead of using the variable frequency modulation method to change the output voltage, the phase shift modulation (PSM) method is adopted in this study. The delay angle between the leading bridge and the following bridge is controlled to modify the output voltage [50]. In this way, the transformer design is less challenging than variable frequency modulation, because the transformer needs over-design for the latter to cover the whole operating frequency range.

TABLE 14. ISOP Converter Detailed Losses

DRU loss (kW)	IGBT loss (kW)	Secondary side DRU loss (kW)	Total loss (kW)
49.5	135	297	481.5

Since the full bridges are grouped in sets of three, there are eight three-phase LLC converters whose inputs are connected in series. Four of these three-phase LLC converters are output parallel connected to one electrolyzer, and the remaining four are connected to another.

The following part analyses the three-phase LLC with 1000 Hz operating frequency since the next section shows that the topology's best operating frequency is around 1000 Hz.

Only one three-phase LLC submodule is built in Simulink, because in steady-state operation, all three-phase LLC submodules should work in the same condition. The designed resonant inductance is 0.11 mH, and the magnetizing inductance is 0.038 H, and the resonant capacitance is 0.22 mF to have a 1000 Hz resonant frequency. The resonant inductance and magnetizing inductance come from the medium frequency transformer. Based on the same design methodology of switches as MMC-SST topology, the primary side inverters switches are chosen as 5SNA 1800E330400 with a voltage rating of 3.3 kV and current rating of 1.8 kA, according to the measured current flowing through the switches. The secondary side diode is chosen as 5SDF28L4521, with three of them in parallel to handle high currents. The input DC capacitance for each full bridge inverter is set as 2.4 mF to limit the voltage ripple, and the output capacitance is set as 32 mF to meet the electrolyzer's 3% current variation requirement. To validate these design choices and demonstrate the system's operational efficacy, the corresponding simulation waveforms are presented in Fig. 18. Specifically, Fig. 18(a) illustrates the sinusoidal resonant current waveforms, while Fig. 18(b) showcases the medium frequency DRU current, which clearly exhibits ZCS characteristics.

Thermal modeling is done for three-phase modules. The resulting losses are multiplied by the number of three phase modules=8. The input 50 Hz DRU losses are directly taken from MMC-SST since both ISOP and MMC-SST have the same input 12 pulse DRU design. As a result, a summary of the losses of different components is shown in Table 14:

The resonant capacitor size and weight estimation are based on the manufacturer datasheet [51]. The size and weight of it are 0.02 m^3 and 28 kg, respectively. The switches' size and weight are 0.003 m^3 and 4.8 kg, respectively. And the input capacitor of 2.4 mF size and weight are estimated as 0.0225 m^3 and 44 kg, based on (3) (4). Adding the size of IGBT and capacitors and leaving margins for other components, the submodule size and weight are estimated as 0.08 m^3 and 100 kg, respectively. The weight value is multiplied by 24 full bridge modules, and the total weight of the submodules is estimated to be 2.4 tons.

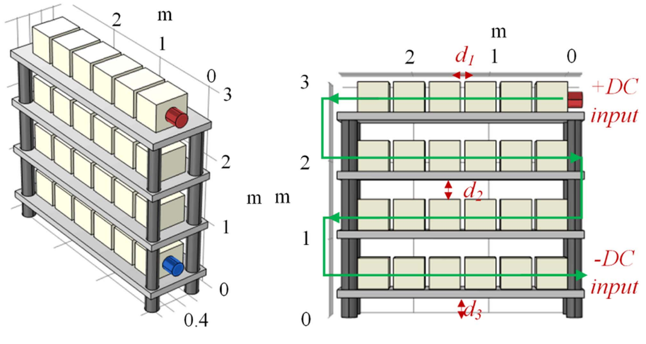

(a) (b)

FIGURE 22. ISOP converter 3D modelling (a) overall structure, (b) side view. There is one converter tower with four rows, each with eight modules.

TABLE 15. ISOP Converter Detailed Size and Weight

ISOP converter size (m^3)	Capacitor weight (ton)	switches weight (ton)	Other Module Weight (ton)
8.94	1.73	0.115	0.557

An insulation design is accomplished for ISOP, as shown in Fig. 22. The red and blue cylinders represent +DC and –DC inputs, respectively. The submodule block dimensions are assumed to be 0.5 m (length) × 0.4 m (width) × 0.4 m (height). Three insulation distances, d_1, d_2, and d_3, have been considered, and the method is the same as MMC-SST, which will not be repeated here. As a result, the total size for the valve tower of ISOP is 0.94 m × 3.15 m × 3.02 m = 8.94 m^3. Table 15 shows a summary of the ISOP converter's size and component weight.

B. DESIGN OF ISOP MFT

The transformer design for this case uses a method similar to the MMR and MMC-SST. However, the number of transformers here is eight. The converter has a square-shaped voltage waveform; thus, the peak voltage must be considered ($U_{pri\text{-}ph\text{-}peak} = 3260$ V). The number of turns in primary and secondary are 10 and 2, respectively. The ISOP is a resonant LLC topology, and it is beneficial to use the leakage inductance of the MFT as the resonant inductor; therefore, the primary and secondary windings are located on top of each other to maintain the desired high leakage inductance, as shown in Fig. 24(a). Another difference is that the ISOP MFT is a shell-type transformer because building the windings as similar as possible is essential, mainly regarding the leakage and magnetizing inductances. Using a shell-type transformer guarantees that the leakage inductances remain similar. The shell-type ISOP MFT is shown in Fig. 24(b).

The cross-section of the core for the MFT at 1000Hz is:

$$A_c = \frac{U_{pri-ph-peak}}{k_c \times k_w \times B_m \times f \times N_p} = \frac{3260}{0.79 \times 4 \times 1.26 \times 1000 \times 10} = 0.082m^2 \qquad (32)$$

Therefore, the core is selected as 2 × 170.2 × 240 mm. The primary and secondary currents are $I_p = 1334$ A and $I_s = 6465$ A, respectively. Therefore, $\mathrm{CTC_{pri}} = 21 \times 13 \times 2 = 546$ mm^2, and $\mathrm{CTC_{sec}} = 5 \times 21 \times 16 \times 2 = 3360$ mm^2 (there are five parallel paths on the secondary side). A 3D view of the ISOP MFT is shown in Fig. 23(a).

TABLE 16. ISOP MFT Detailed Losses

Copper loss (kW)	Core loss (kW)	Stray loss (kW)	Total losses (kW)
644.8	64.6	96.9	806.3

TABLE 17. ISOP MFT Detailed Size and Weight

Transformer size (m^3)	Copper weight (ton)	Core weight (ton)	tank weight (ton)	Oil weight (ton)
13.78	4.4	15.8	1.74	6.86

TABLE 18. FEM Results for ISOP MFTs

Frequency	Parameter	Value
1000 Hz	L_{lk}	110.4 uH
	r_p	475.49 μΩ/m
	r_s	88.903 μΩ/m

1) INSULATION AND THERMAL CONSIDERATIONS

The insulation and thermal considerations for ISOP MFT are similar to those for MMC-SST and MMR. To decrease the insulation stress, the cores are clamped to the middle point of the input DC Bus and insulated from the tank accordingly. There are eight active parts inside one tank, as shown in Fig. 23(b) and (c).

2) OVERALL METRICS OF THE ISOP MFT

The transformers' detailed loss, total size, and weight breakdown are shown in Tables 16 and 17. The FEM simulation results for ISOP MFT are summarized in Table 18.

The loss, size, and weight information for the power converter, MFTs, and chiller for ISOP at 1000 Hz are summarized in Table 8.

C. PERFORMANCE METRICS AT DIFFERENT FREQUENCIES

Following a similar analysis process, the losses, sizes, and weights of the ISOP topologies at different frequencies are shown in Fig. 15(c). Due to the ZVS turn-on characteristics, turn-on losses are effectively eliminated. However, turn-off losses are still present and contribute to the overall power loss observed in the converter. As a result, the converter power loss fluctuates between different frequencies, as observed in Fig. 15(c).

As indicated in Fig. 15(c), the optimal fundamental frequency for the ISOP topology is set at approximately 1000 Hz, with a primary focus on reducing size and weight.

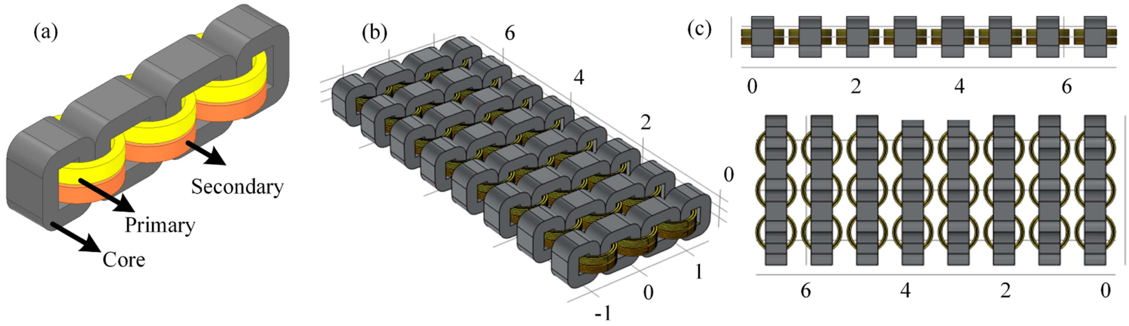

FIGURE 23. The ISOP MFT: (a) the 3D view of one MFT, (b) the 3D view of the eight MFTs inside the tank, and (c) the side views.

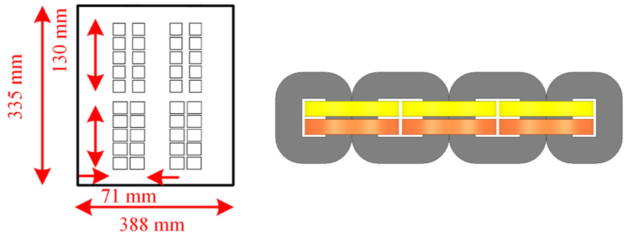

(a) (b)

FIGURE 24. Details of the ISOP transformer design: (a) ISOP MFT window, (b) ISOP shell-type transformer with windings on top of each other.

V. TOPOLOGIES COMPARISON RESULTS

Sections II, III, and IV have thoroughly detailed the design processes for the MMC-SST, MMR-SST, and ISOP-SST, respectively, with summarized results presented in Fig. 15. To determine the most suitable topology for electrolyzer applications, this section begins with a frequency sweep analysis for each topology. Subsequently, a comparison of the three topologies at their optimal operating frequencies is performed.

A. FREQUENCY SWEEP ANALYSIS

Fig. 15(a)-(c) illustrates the frequency sweep analyses for MMC-SST, MMR, and ISOP topologies, focusing on their loss, size, and weight characteristics. In all three topologies, converter and transformer losses each account for approximately half of the total losses. Specifically, due to the hard switching operation of the MMC-SST, converter losses increase linearly with the operating frequency as the switching losses are directly proportional to frequency. In contrast, for MMR and ISOP, which feature soft-switching characteristics, converter losses are significantly reduced. However, switching losses are not completely eliminated. For MMR, due to the DC bias of the MMC arm current, switching losses persist, as detailed in the loss analysis in Section III-A. For ISOP, while Zero-Voltage Switching (ZVS) turn-on characteristics eliminate turn-on losses, turn-off losses remain. Consequently, within a certain frequency range, here identified as 1000Hz, converter losses are maintained at a relatively low level. Beyond this frequency, however, converter losses increase sharply, pushing switch junction temperatures beyond safe operational limits.

In terms of transformer losses, the trend differs: losses initially decrease and then increase with rising frequencies. This is due to the reduction in core size with higher frequencies, which lowers core losses and reduces the Mean Length per Turn, thus decreasing copper losses. However, increased frequencies also intensify losses in the windings due to the proximity effect and skin effect, causing transformer losses to vary with frequency.

In terms of size and weight trends, there is a discernible pattern where both transformer size and weight are inversely proportional to the operating frequency. For MMC-SST, beyond approximately 400 Hz, and for MMR and ISOP, beyond around 1000 Hz, the transformer size becomes negligible compared to that of the chiller. In these three topologies, transformer weight is typically the dominant factor; however, at higher frequencies, the weight of the chiller becomes increasingly significant. Regarding the converter section, attention is given to how changes in frequency affect the size and weight of capacitors. In this frequency sweep analysis, the impact of capacitor size and weight is minimal and does not significantly influence the determination of the optimal operating frequency.

B. ANALYSIS OF TOPOLOGIES AT OPTIMAL FREQUENCIES

As detailed in Section II-E, III-C, and IV-C, when prioritizing size and weight reduction, the optimal operating frequencies for the MMC, MMR, and ISOP topologies have been identified as 400 Hz, 1000 Hz, and 1000 Hz, respectively. Fig. 15(d) presents a comparison of these topologies' performance metrics at their respective optimal frequencies.

Among the designs evaluated, the MMC-SST is the bulkiest and heaviest, and it also exhibits the highest energy losses. In contrast, the ISOP-SST and MMR-SST excel in different aspects: the ISOP-SST achieves the lowest losses and is the most compact, while the MMR-SST is distinguished by having the lowest weight.

In terms of loss comparison, transformer copper loss constitutes a significant portion of the total losses. The MMR and ISOP experience higher copper losses than the MMC-SST due to their higher operating frequencies, which intensify the proximity effect. Regarding IGBT losses, the ISOP-SST benefits from reduced switching losses owing to its soft-switching capabilities. In contrast, the MMR-SST does not achieve full soft switching, attributed to the DC bias in its arm current. Concerning conduction losses, the different current ratings of the IGBTs used lead to variations: ISOP employs 1800A IGBTs due to higher current requirements, whereas MMR uses 1200A IGBTs. Consequently, the total losses for MMC-SST and MMR are comparable, while the total loss for ISOP is slightly lower.

In all three topologies, the chiller size is a dominant factor. The ISOP-SST stands out for its compactness, largely due to its reduced module count, resulting in smaller converter towers. Specifically, the MMR topology requires 144 submodules distributed across multiple racks, necessitating ample space between racks for maintenance. In contrast, the ISOP system comprises only 24 modules, which can be accommodated within a single rack. This configuration significantly reduces the required insulation and maintenance space, as illustrated in Fig. 24, thereby minimizing the overall size of the converter compared to the other two scenarios.

Regarding weight, the chiller and core weights are significant factors across all three topologies. The MMR topology features a notably lighter core, achieved by using only two 1000 Hz transformers, as opposed to the eight utilized in ISOP-SST. This design choice reflects the principle that a single, larger transformer tends to be more weight-efficient than multiple smaller units, offering substantial weight savings.

VI. CONCLUSION

This paper comprehensively designs and compares the MMC-based, MMR-based, and ISOP SST for electrolyzer applications from the efficiency, size, and weight points of view. The size of the converter towers and transformers are calculated with practical considerations, including the insulation distance requirements.

Based on the detailed analysis provided, five key findings emerge:

1) The analysis emphasizes the critical role of chiller size and weight in evaluating each topology, underscoring the importance of considering these factors in size and weight comparisons.
2) The adoption of a soft-switching topology is recommended to achieve lower converter losses, which in turn reduces the size and weight of the chiller due to decreased cooling requirements.
3) A lower number of submodules typically necessitates reduced insulation and maintenance space, consequently diminishing the overall size of the converters.
4) Topologies utilizing a central transformer generally exhibit lower transformer size and weight compared to those employing multiple smaller transformers.
5) Within the specific application context and ratings investigated, the ISOP-SST emerges as the optimal choice for applications where space conservation is crucial, whereas the MMR-SST is found to be more suitable for scenarios where minimizing weight is a critical consideration.

While the design procedures and evaluation work in this study were conducted under specific parameters, the analytical framework employed for calculating and comparing losses, size, and weight across different topologies, especially through the frequency sweep method, demonstrates high adaptability. This versatility enables the framework to be effectively applied to various system parameters, offering a robust guideline for adapting to diverse operational conditions and application scenarios.

APPENDIX

A. INSULATION DESIGN OF THE MMC-SST CONVERTER

In the 3D design shown in Fig. 6, four insulation distances have been analyzed.

- The distance between modules d_1:

The standard rated lightning impulse withstand voltage for the voltage difference between modules $U_{dc}/2/N_{sm}$=23.1 kV / 24 = 0.96 kV is 40 kV. And the minimum clearance for 40 kV standard-rated lightning impulse withstand voltage is 60 mm, which is set as d_1.

- The distance between the rows of the converter towers d_2:

The voltage difference between rows is 23.1 kV/24×16=15.4 kV, and the required lightning impulse withstand voltage is 95 kV. The insulator is placed between different rows, and based on the manufacturer datasheet [52], the height of the insulator corresponding to 95 kV withstand voltage is 255mm, which is set as d_2.

- The distance between the lower row and the ground d_3:

The maximum output phase voltage is $U_{dc}/2$=23.1 kV, which is the voltage difference between the lower row and the ground. The required lightning impulse withstand test is 95 kV. The insulator height is the same as in the previous section to estimate the distance between the rows. Thus, d_3 is set as 255 mm.

- The distance between the converter towers d_4:

The voltage difference between the converter towers of the same phase is 46.2 kV DC, which is equivalent to an AC RMS voltage of 32.7 kV. The required lightning impulse withstand voltage is 170 kV peak, and the required clearance is 32 cm. However, this value is increased to 1 m for easy maintenance in case of module failure.

Considering the above insulation distance, the total size is 6.86 m × 3.22 m × 1.95 m = 43 m^3.

B. MFT INSULATION FEM SIMULATIONS

To satisfy the insulation distances d_1 to d_4 in Fig. 11, these distances between the active parts (MFTs) and the walls of the transformer tank are determined by considering three main factors:

TABLE 19. Permissible Filed Strength in at the Critical Points of an Oil-Type Transformer [55]

No	Critical point		Electric field (kV/mm)
1	Oil, between barriers		10
2	Oil, along interfaces		< 5
3	Oil-impregnated paper	Perpendicular to layers	30 ~ 60
4		Parallel to layers	6 ~ 10

1) Electrical Clearance: ensuring adequate clearance to prevent dielectric breakdown in the transformer oil, following the standards set by IEC 60156 [53].
2) Thermal Management: Adequate spacing is critical for effective heat dissipation, which is vital given the thermal characteristics of the transformer oil compared to air.
3) Mechanical Stability and Safety: accounting for sufficient space to accommodate thermal expansion of the oil and other components like the core and windings.

Among these factors, thermal management is predominant. The permissible fields within the oil-type transformer at critical locations are carefully considered to ensure a reliable operation , as summarized in Table 19.

Given the inherent uncertainties in these figures, a safety margin is crucial. Considering the maximum allowable electric field within the transformer oil to be 5 kV/mm and implementing a safety margin, the maximum electric field is 2.5 kV/mm. This conservative approach is further reinforced by the calculation for the minimum required gap between the windings and the tank, based on the peak of the maximum applied test voltage ($\sqrt{2} \times 70\ \text{kV} \approx 100\ \text{kV}$), resulting in:

$$G_{\min} = \frac{V_{test\_\max}}{E_{oil\_\max}} = \frac{100}{2.5} = 40\text{mm} \tag{33}$$

where G_{min} is the minimum required gap, V_{test_max} is the peak of maximum applied test voltage, and E_{oil_max} is the maximum of permissible electric field inside the oil. Then $d_1 - d_4$ must be greater than G_{min}.

However, to ensure sufficient spacing for the effective laminar flow of oil, which is critical for both cooling and electrical insulation purposes, in this design d_1, d_2, and d_4 are selected as 100 mm—significantly exceeding the minimum requirement. Also, d_3 is selected as 300 mm to guarantee enough spacing on top of the transformer for convection heat dissipation. This extra spacing helps mitigate any potential risk associated with the alignment and positioning of the internal components during operation and maintenance, thereby enhancing the overall system reliability and robustness.

The FEM simulation of the electric filed is shown in Fig. 25, which indicates the electric filed between the primary winding and core, and between disks of the primary winding, and between turns of a disk regarding the values of Table 19.

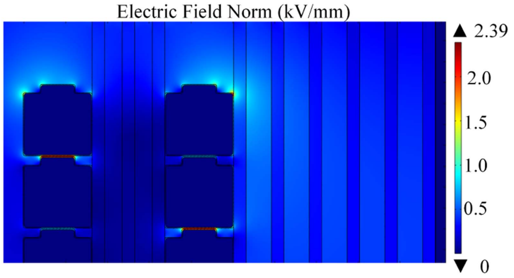

FIGURE 25. The FEM simulation of electric filed.

REFERENCES

[1] B. L. Nguyen, M. Panwar, R. Hovsapian, K. Nagasawa, and T. V. Vu, “Power converter topologies for electrolyzer applications to enable electric grid services,” in *Proc. IEEE 47th Annu. Conf. IEEE Ind. Electron. Soc.*, 2021, pp. 1–6.

[2] R. Mirzadarani et al., “Three-phase medium-voltage medium-frequency transformer for SST in green hydrogen production,” in *Proc. IEEE 49th Annu. Conf. Ind. Electron. Soc.*, 2023, pp. 1–6, doi: 10.1109/IECON51785.2023.10312546.

[3] B. Yodwong, D. Guilbert, M. Phattanasak, W. Kaewmanee, M. Hinaje, and G. Vitale, “AC-DC converters for electrolyzer applications: State of the art and future challenges,” *Electronics*, vol. 9, no. 6, 2020, Art. no. 912.

[4] E. S. Lee, J. H. Park, M. Y. Kim, and J. S. Lee, “High efficiency module design of solid-state transformers for railway vehicles,” *IEEE Trans. Transp. Electrific.*, vol. 8, no. 1, pp. 98–120, Mar. 2022.

[5] P. Kjaer, Y. Chen, and C. Dincan, “DC collection: Wind power plant with medium voltage dc power collection network,” presented at the ECPE Workshop on Smart Transformers for Traction and Future Grid Applications, Zurich, Switzerland, Feb. 2016.

[6] I. Syed and V. Khadkikar, “Replacing the grid interface transformer in wind energy conversion system with solid-state transformer,” *IEEE Trans. Power Syst.*, vol. 32, no. 3, pp. 2152–2160, May 2017.

[7] N. Doerry and K. McCoy, “Next generation integrated power system: NGIPS technology development roadmap,” *Nav. Sea Syst. Command*, Washington, DC, USA, Tech. Rep. SER-05D/349, 2007.

[8] Y. Du, S. Baek, S. Bhattacharya, and A. Q. Huang, “High-voltage high-frequency transformer design for a 7.2 kV to 120V/240V 20kVA solid state transformer,” in *Proc. IEEE 36th Annu. Conf. Ind. Electron. Soc.*, 2010, pp. 493–498.

[9] T. Zhao, G. Wang, S. Bhattacharya, and A. Q. Huang, “Voltage and power balance control for a cascaded H-bridge converter-based solid-state transformer,” *IEEE Trans. Power Electron.*, vol. 28, no. 4, pp. 1523–1532, Apr. 2013, doi: 10.1109/tpel.2012.2216549.

[10] C. Lu, W. Hu, H. Wu, and F. C. Lee, “Quasi-two-level bridgeless PFC rectifier for cascaded unidirectional solid state transformer,” *IEEE Trans. Power Electron.*, vol. 36, no. 10, pp. 12033–12044, Oct. 2021.

[11] Z. Pei et al., “Hybrid isolated modular multilevel converter based solid-state transformer topology with simplified power conversion process and uneven voltage ratio,” *IEEE Trans. Power Electron.*, vol. 38, no. 10, pp. 12757–12773, Oct. 2023, doi: 10.1109/TPEL.2023.3295059.

[12] Z. Bu, W. Zhao, M. Zhang, J. Teng, X. Li, and X. Sun, “Dynamic performance evaluation and optimization of common HFAC bus lightweight MMC-SST,” *IEEE Trans. Power Electron.*, vol. 39, no. 2, pp. 2035–2050, Feb. 2024, doi: 10.1109/TPEL.2023.3326288.

[13] G. Zheng, Y. Chen, and Y. Kang, “A modular multilevel converter (MMC) based solid-state transformer (SST) topology with simplified energy conversion process and magnetic integration,” *IEEE Trans. Ind. Electron.*, vol. 68, no. 9, pp. 7725–7735, Sep. 2021, doi: 10.1109/TIE.2020.3013493.

[14] Z. Li et al., “Comparison of modular multilevel converter based solid state transformer for AC/DC application,” in *Proc. IEEE 49th Annu. Conf. Ind. Electron. Soc.*, 2023, pp. 1–6, doi: 10.1109/IECON51785.2023.10312314.

[15] Z. Lu, L. Lin, X. Wang, and C. Xu, “LLC-MMC resonant DC-DC converter: Modulation method and capacitor voltage balance control strategy,” in *Proc. IEEE Appl. Power Electron. Conf. Expo.*, 2020, pp. 2056–2061, doi: 10.1109/APEC39645.2020.9124312.

[16] H. Saeedifard and A. Yazdani, “Modeling and soft-switching operation of an isolated modular-multilevel-converter-based DC-DC converter,” in *Proc. IEEE Energy Convers. Congr. Expo.*, 2022, pp. 1–8, doi: 10.1109/ECCE50734.2022.9947871.

[17] S. Belkhode, P. Rao, A. Shukla, and S. Doolla, “Comparative evaluation of silicon and silicon-carbide device-based MMC and NPC converter for medium-voltage applications,” *IEEE J. Emerg. Sel. Topics Power Electron.*, vol. 10, no. 1, pp. 856–867, Feb. 2022, doi: 10.1109/JESTPE.2021.3103075.

[18] G. Abeynayake, G. Li, T. Joseph, J. Liang, and W. Ming, “Reliability and cost-oriented analysis, comparison and selection of multilevel MVDC converters,” *IEEE Trans. Power Del.*, vol. 36, no. 6, pp. 3945–3955, Dec. 2021, doi: 10.1109/TPWRD.2021.3051531.

[19] S. Shao et al., “A modular multilevel resonant DC–DC converter,” *IEEE Trans. Power Electron.*, vol. 35, no. 8, pp. 7921–7932, Aug. 2020, doi: 10.1109/TPEL.2019.2962032.

[20] Z. Yi, S. Shaolei, DianguoXu, and Y. Rongfeng, “Comparison and review of DC transformer topologies for HVDC and DC grids,” in *Proc. IEEE 8th Int. Power Electron. Motion Control Conf.*, 2016, pp. 3336–3343, doi: 10.1109/IPEMC.2016.7512830.

[21] L. Camurca, T. Pereira, F. Hoffmann, and M. Liserre, “Analysis, limitations, and opportunities of modular multilevel converter-based architectures in fast charging stations infrastructures,” *IEEE Trans. Power Electron.*, vol. 37, no. 9, pp. 10747–10760, Sep. 2022, doi: 10.1109/TPEL.2022.3167625.

[22] A. Marzoughi, R. Burgos, D. Boroyevich, and Y. Xue, “Design and comparison of cascaded H-bridge, modular multilevel converter, and 5-L active neutral point clamped topologies for motor drive applications,” *IEEE Trans. Ind. Appl.*, vol. 54, no. 2, pp. 1404–1413, Mar./Apr. 2018, doi: 10.1109/TIA.2017.2767538.

[23] B. Zhao, Q. Song, J. Li, X. Xu, and W. Liu, “Comparative analysis of multilevel-high-frequency-link and multilevel-DC-link DC–DC transformers based on MMC and dual-active bridge for MVDC application,” *IEEE Trans. Power Electron.*, vol. 33, no. 3, pp. 2035–2049, Mar. 2018, doi: 10.1109/TPEL.2017.2700378.

[24] Infineon, “Bipolar semiconductor-technical information,” Infineon Technologies Bipolar GmbH & Co. KG, Warstein, Germany, 2012, Accessed: Jun. 1, 2024. [Online]. Available: https://community.infineon.com/gfawx74859/attachments/gfawx74859/twdiodethyristors/68/1/Infineon%20Bipolar%20-%20AN20012-01%20-%20Technical%20Information.pdf

[25] I. G. Park and S. I. Kim, “Modeling and analysis of multi-interphase transformers for connecting power converters in parallel,” in *Proc. IEEE Rec. 28th Annu. Power Electron. Specialists Conf.. Formerly Power Conditioning Specialists Conf. 1970-71. Power Process. Electron. Specialists Conf. 1972*, 1997, vol. 2, pp. 1164–1170, doi: 10.1109/PESC.1997.616895.

[26] T. E. Slettbakk, “Development of a power quality conditioning system for particle accelerators,” Norwegian University of Science and Technology, Trondheim, Norway, CERN-THESIS-2018-337, 2018.

[27] K. Sharifabadi, L. Harnefors, H.-P. Nee, S. Norrga, and R. Teodorescu, *Design, Control and Application of Modular Multilevel Converters for HVDC Transmission Systems*. Hoboken, NJ, USA: Wiley, 2016, pp. 1–386.

[28] *Power transformers - Part 1: General*, Standard IEC 60076-1, IEC: Geneva, Switzerland, 2011.

[29] ELECTRONICON, “E57 /E59 / SR17TM AC and DC capacitors with large capacitances,” ELECTRONICON Kondensatoren GmbH, Gera, Germany, 2022, Accessed: Jun. 1, 2024. [Online]. Available: https://www.electronicon.com/fileadmin/inhalte/PDF-Dateien/Kataloge_und_Broschueren/200.003-020070_E56-SR17.pdf

[30] Hitachi, “Dry capacitors for voltage source converters,” Hitachi Energy, Ludvika, Sweden, 2022, Accessed: Jun. 1, 2024. [Online]. Available: https://library.e.abb.com/public/a80941e7c2484e03b9cd0ffaf76cc0e7/Hitachi_Energy_DryDcap.pdf?x-sign=Ovm9IaMEpmct/UFHZR8PDF2rsuH7uXu80kBwLoK4IQaRDrrAtpPCDoAlCsOyfKN7

[31] G. P. Lourduraj, “Feasibility study of oil immersed power electronic based high voltage test source for onsite testing purpose,” M.S. thesis, Electrical Engineering, Mathematics and Computer Science, TU Delft, Delft, The Netherlands, 2019.

[32] M. J. H. P. Franklin, *The J & P Transformer Book : A Practical Technology of the Power Transformer*. Burlington, MA, USA: Newnes, 2007.

[33] J. H. Harlow, *Electric Power Transformer Engineering*. New York, NY, USA: Taylor & Francis, 2012.

[34] Metglas, “Magnetic materials,” metglas.com, 2017. Accessed: Dec. 09, 2023. [Online]. Available: https://metglas.com/magnetic-materials/

[35] S. Meier, T. Kjellqvist, S. Norrga, and H. P. Nee, “Design considerations for medium-frequency power transformers in offshore wind farms,” in *Proc. 13th Eur. Conf. Power Electron. Appl.*, 2009, pp. 1–12.

[36] C. Yang, H. Hu, P. Tian, J. Shi, Z. Wang, and C. Zhang, “Study on the loss characteristics of dry-type power transformers considering stray losses,” in *Proc. IEEE 4th China Int. Youth Conf. Elect. Eng.*, 2023, pp. 1–5, doi: 10.1109/CIYCEE59789.2023.10401766.

[37] B. Liu, Y. Takahashi, K. Fujiwara, and S. Imamori, “Stray loss evaluation of power transformers using simplified air-core model with tank and frame,” *IEEE Trans. Magn.*, vol. 59, no. 11, Nov. 2023, Art. no. 8401606, doi: 10.1109/TMAG.2023.3288893.

[38] K.-H. Park, H.-J. Lee, and S.-C. Hahn, “Finite-element modeling and experimental verification of stray-loss reduction in power transformer tank with wall shunt,” *IEEE Trans. Magn.*, vol. 55, no. 12, Dec. 2019, Art. no. 7502104, doi: 10.1109/TMAG.2019.2940825.

[39] B. P. J. Duc, M. Aguirre, and P. Gutirrez, “Loss prophet, predicting stray losses in power transformers and optimization of tank shielding using FEM,” ABB, 2016. [Online]. Available: https://library.e.abb.com/public/9eb08c572459433e996a97df264d1df6/51-56%204m6053_EN_72dpi.pdf

[40] X. M. Lopez-Fernandez and L. A. Alvarez-Gomez, “Calculation of stray losses in continuously transposed conductor cable transformer windings by multi-slice methodology,” *Int. J. Elect. Power Energy Syst.*, vol. 111, pp. 25–33, 2019, doi: 10.1016/j.ijepes.2019.03.038.

[41] *POWER TRANSFORMERS – Part 2: Temperature rise for liquid-immersed transformers*, Standard IEC 60076-2, IEC: Geneva, Switzerland, 2011.

[42] B. P. Robert, M. D. Vecchio, P. T. Feghali, D. M. Shah, and R. Ahuja, *Transformer Design Principles*, 3rd ed. Boca Raton, FL, USA: CRC, 2018.

[43] L. W. Pierce, “An investigation of the thermal performance of an oil filled transformer winding,” *IEEE Trans. Power Del.*, vol. 7, no. 3, pp. 1347–1358, Jul. 1992, doi: 10.1109/61.141852.

[44] D. Susa and M. Lehtonen, “Dynamic thermal modeling of power transformers: Further development-Part II,” *IEEE Trans. Power Del.*, vol. 21, no. 4, pp. 1971–1980, Oct. 2006, doi: 10.1109/TPWRD.2005.864068.

[45] *Power Transformers - Part 3: Insulation Levels, Dielectric Tests and External Clearances in Air*, Standard IEC 60076-3, IEC: Geneva, Switzerland, 2018.

[46] DeltaTemp, “Industrial cooling & climation,” delta-temp.com, 2020. Accessed: Dec. 18, 2023. [Online]. Available: https://www.delta-temp.com/en/

[47] K. H. Chen, J. Y. Lin, Y. F. Lin, Y. C. Chang, and H. J. Chiu, “Design of three phase wye-delta LLC converter with time domain analysis,” in *Proc. 10th Int. Conf. Power Electron. ECCE Asia*, 2019, pp. 1–6, doi: 10.23919/ICPE2019-ECCEAsia42246.2019.8797258.

[48] H. Huang, “Designing an LLC resonant half-bridge power converter,” in *Proc. Texas Instruments Power Supply Des. Seminar,* 2010, vol. 3, pp. 2010–2011.

[49] Y. Nakakohara, H. Otake, T. M. Evans, T. Yoshida, M. Tsuruya, and K. Nakahara, “Three-phase LLC series resonant DC/DC converter using SiC MOSFETs to realize high-voltage and high-frequency operation,” *IEEE Trans. Ind. Electron.*, vol. 63, no. 4, pp. 2103–2110, Apr. 2016, doi: 10.1109/TIE.2015.2499721.

[50] K. Murata and F. Kurokawa, “An interleaved PFM LLC resonant converter with phase-shift compensation,” *IEEE Trans. Power Electron.*, vol. 31, no. 3, pp. 2264–2272, Mar. 2016, doi: 10.1109/TPEL.2015.2427735.

[51] zez-silko, “Induction heating capacitors,” zez-silko.com, 2021. Accessed: Dec. 18, 2023. [Online]. Available: https://www.zez-silko.com/induction-heating

[52] P. insulators, “BIL 60-95 kV,” ppcinsulators.com, 2018. Accessed: Dec. 18, 2023. [Online]. Available: https://www.ppcinsulators.com

[53] *Insulating Liquids - Determination of the Breakdown Voltage at Power Frequency - Test Method*, Standard IEC 60156, IEC: Geneva, Switzerland, 2018.

[54] *Fluids for Electrotechnical Applications – Mineral Insulating Oils for Electrical Equipment*, Standard IEC 60296, IEC: Geneva, Switzerland, 2020.

[55] F. H. Kreuger, *Industrial High Voltage /[Vol. III], Industrial High DC Voltage: 1. Fields, 2. Breakdowns 3. Tests*. Delft, The Netherlands: Delft Univ. Press, 1995.